Dendritic ridges in Antoniadi basin, Mars: Fluvial or volcanic landforms?

N. Mangold, A. Guimpier, L.L. Tornabene, S.J. Conway, P. Fawdon, E. Hauber, A. Noblet, A.S. Zaki, A. Pommerol, N. Thomas

Icarus 406 (2023) 115735

Contents lists available at ScienceDirect

Icarus

journal homepage: www.elsevier.com/locate/icarus

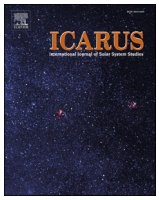

Dendritic ridges in Antoniadi basin, Mars: Fluvial or volcanic landforms?

N. Mangold [a,*], A. Guimpier [a], L.L. Tornabene [b], S.J. Conway [a], P. Fawdon [c], E. Hauber [d], A. Noblet [a,b], A.S. Zaki [e], A. Pommerol [f], N. Thomas [f]

[a] LPG, CNRS, Nantes Université, Université Angers, Le Mans Université, 44322 Nantes, France
[b] Institute for Earth and Space Exploration, University of Western Ontario, Dept. of Earth Sciences, 1151 Richmond Street, London, Ontario N6A 5B7, Canada
[c] School of Physical Science, The Open University, Milton Keynes, UK
[d] DLR, Berlin, Germany
[e] Department of Earth Sciences, University of Geneva, 1205 Geneva, Switzerland
[f] Universität Bern, Physikalisches Institut, Switzerland

ARTICLE INFO

Keywords:
Mars
CaSSIS
HRSC
Volcanic
Fluvial

ABSTRACT

Antoniadi basin displays dark-toned dendritic ridges previously interpreted as inverted fluvial channels. Detailed observations of these dark-toned ridges as well as the geological units in the central region of Antoniadi basin are provided emphasizing images from the Colour and Stereo Surface Imaging System (CaSSIS), the High Resolution Stereo Camera (HRSC) and the High Resolution Imaging Science Experiment (HiRISE) instruments. Results show that the dark-toned ridges are part of the most recent geological unit as they overlie, and thus postdate all plains of the central Antoniadi basin, which is Early Amazonian based on its crater size-frequency distribution. Our observations of the dark-toned ridges are not consistent with inverted fluvial channels: they do not widen in the expected downstream direction, they display a rubbly texture and lack layering at high resolution, and have lobes with local levees in place of channel heads. In addition, the branched ridges are more mafic in composition and display a relatively higher thermal inertia than their surroundings. This suite of characteristics is better explained by volcanic flows developed as distributary channels rather than fluvial tributary channels. The occurrence of dikes in the east and west of the studied region supports that these flows were formed by lava, perhaps a'a like flows as suggested by the rubbly texture, but with an unusually high degree of digitation. Alternatively, such a geometry could be explained by the emplacement of the lava along pre-existing fluvial valleys, but neither the underlying topography, nor two nearby older craters, exhibit signs of fluvial erosion.

1. Introduction

Fluvial systems, and their sedimentary deposits, are key landforms for understanding the geologic history and evolution of the past climate on Mars. Among these landforms, inverted and exhumed channels are noteworthy, because they show the presence of fluvial activity in regions where fluvial erosion did not incise the bedrock but instead deposited sediments, such as in alluvial plains, delta plains or alluvial fans, and are thus valuable paleoclimate indicators (e.g., Pain and Ollier, 1995). Inverted channels have been reported on Mars, in various contexts and not exclusively within Noachian-aged, but also younger terrains, such as Valles Marineris plateau, Zephyria plains or Arabia Terra highlands (e.g., Mangold et al., 2008; Burr et al., 2010; Davis et al., 2016; Zaki et al., 2021). Thus, identifying well-developed networks of inverted channels is of importance to characterize the type of aqueous processes involved and their extent in space and time. Antoniadi Basin is a Middle Noachian aged (Werner, 2008, Robbins et al., 2013) impact basin that has experienced several episodes of fluvial activity, including a tentative late stage as evidenced by possible inverted channels (Figs. 1-3) (Zaki et al., 2020). These possible inverted channels have a dendritic pattern in plan view.

A solid conclusion cannot be drawn from the visual identification of a dendritic pattern alone. Although dendritic landforms are traditionally considered as hallmarks of fluvial processes on Earth, several processes can produce similar landforms (De Blasio, 2022). For such cases, it is important to remain agnostic in regards to the process that may have shaped these landforms. However, constraints can be put on the processes that most likely contributed to the formation of these surface features through observations across multiple datasets and integration of geomorphological observations with the local and regional context.

* Corresponding author.
E-mail address: nicolas.mangold@univ-nantes.fr (N. Mangold).

https://doi.org/10.1016/j.icarus.2023.115735
Received 28 March 2023; Received in revised form 28 June 2023; Accepted 31 July 2023
Available online 2 August 2023

Thus, we will use a non-genetic term, "branched ridges", for these landforms throughout the observation sections of the manuscript. After a description of the utilized datasets, we present the geological context of the Antoniadi basin, then describe the geological units and landforms, and focus on both their relative and absolute ages. A specific focus on the geometry of the branching ridges is provided before discussing their origin.

2. Datasets

Geomorphological interpretations are made using images in visible and near infrared wavelengths from the Colour and Stereo Surface Imaging System (CaSSIS, Thomas et al., 2017) onboard Trace Gas Orbiter of ExoMars, the High Resolution Stereo Camera (HRSC, Neukum et al., 2004) onboard the Mars Express probe, from both the Context Camera (CTX, Malin et al., 2007) and the High Resolution Imaging Science Experiment (HiRISE, McEwen et al., 2007) onboard Mars Reconnaissance Orbiter, and the Thermal Emission Imaging System (THEMIS, Christensen et al., 2004) instrument onboard Mars Odyssey. CaSSIS data provide color/multispectral information, which can be used to put some general constraints on the composition of the surface (Thomas et al., 2017; Tornabene et al., 2018a). The estimated band centers for the four CaSSIS broadband filters (as reported in the latest data release image headers and based on radiometric calibration v1.2) are: 495 (blue-green color, BLU), 678 nm (a broader "panchromatic" red filter, PAN), 836 nm (named RED, although in the infrared) and 939 nm (for the near-infrared, NIR) (Thomas et al., 2017). The two first bands, BLU and PAN are close to the first two bands used by HiRISE ensuring a consistent use of colors between the CaSSIS and HiRISE datasets; the two other CaSSIS filters, RED and NIR, split the HiRISE IR filter (~900 nm) into two filters designed, and have since been demonstrated (Tornabene et al., 2018a), to better discriminate between Fe-bearing phases, such as ferrous iron Fe^{2+} (mafic minerals) or ferric iron Fe^{3+} (hematite, etc.).

Mars Orbiter Laser Altimeter (MOLA, Smith et al., 2001) gridded data were used to extract regional topography. For local observations, a DEM was constructed using HiRISE stereo image pairs on the branched ridges. This DEM was produced by stereophotogrammetry using USGS ISIS3 and BAE SocetSet software, with a spatial gridding of 1 m/pixel and an estimated vertical precision of 0.35 m (Kirk et al., 2003, 2008). This DEM is available on the PDS and from the HiRISE web page (https://www.uahirise.org/dtm/dtm.php?ID=ESP_057678_2015).

3. Geological context

Antoniadi basin is a 330 km diameter impact basin localized in the east of Arabia Terra and dated from the Early to Middle Noachian (~3.9 Gy, Werner, 2008, Robbins et al., 2013). Given the diameter, this basin was initially > > 5 km deep (e.g. Melosh, 1989). The basin rims currently have a maximum of 1.8 km of elevation above the floor, but in many locations they are only 500 m above the floor (Fig. 1), suggesting both erosion of the rim and substantial infilling by volcanic, impact and/or sedimentary material, as observed for many Noachian basins on Mars.

Fluvial landforms have been observed on the basin's western and northern rim, with associated depositional fans and layered deposits (Zaki et al., 2020), which could have contributed to the erosion of rims. However, the interior of the basin appears to be devoid of fluvial landforms or obvious sedimentary deposits, with the possible exception of the dendritic features that are the focus of our study (Zaki et al., 2020; Mangold et al., 2021). These branched ridges are located close to the center of the basin, 20 km south of crater B, and 60 km south of the filled crater A (Fig. 2).

In the central part of Antoniadi basin where these ridges are observed, the crater floor is generally featureless at km-scale, with exception of small impact craters and wrinkle ridges. In the southern part of the basin, a number of platy landforms and linear ridges are visible (Fig. 1c), as expected in volcanic flood plains and observed in other regions of Mars (e.g., Vaucher et al., 2009), and in agreement with the global mapping suggesting lava plains (Fig. 1b). Antoniadi basin lies at the margin of the Syrtis Major Planum volcanic province (Fig. 1). Global scale mapping (Tanaka et al., 2014) suggests that the surface of Antoniadi basin is a continuation of lava flows from Syrtis Major Planum. While there is a shallow spillway into the crater (Fig. 1b) substantial flooding of Antoniadi basin is not supported by the crater floor topography (Hiesinger and Head, 2004; Fawdon, 2016). As such, it is likely that that only relatively minor volumes of lava where transported from the plains of Syrtis Major Planum, but that most lavas may have been directly sourced from the periphery of the plume that fed Syrtis Major (i.e., from directly underneath Antoniadi, Fawdon, 2016).

4. Observations

4.1. Main geological units, landforms and structures

The purpose of this sub-section is to provide a detailed description of the geological units and features in central Antoniadi basin. Given the scarcity of high-resolution imaging, we do not provide an exhaustive mapping of all landforms. We provide a context map at HRSC scale extrapolated from local observations at HiRISE and CaSSIS scales to localize the observed units and features of interest with respect to the stratigraphy and structural history of the Antoniadi basin (Figs. 1-2). A more detailed description of the branched ridges is provided in section 4.2.

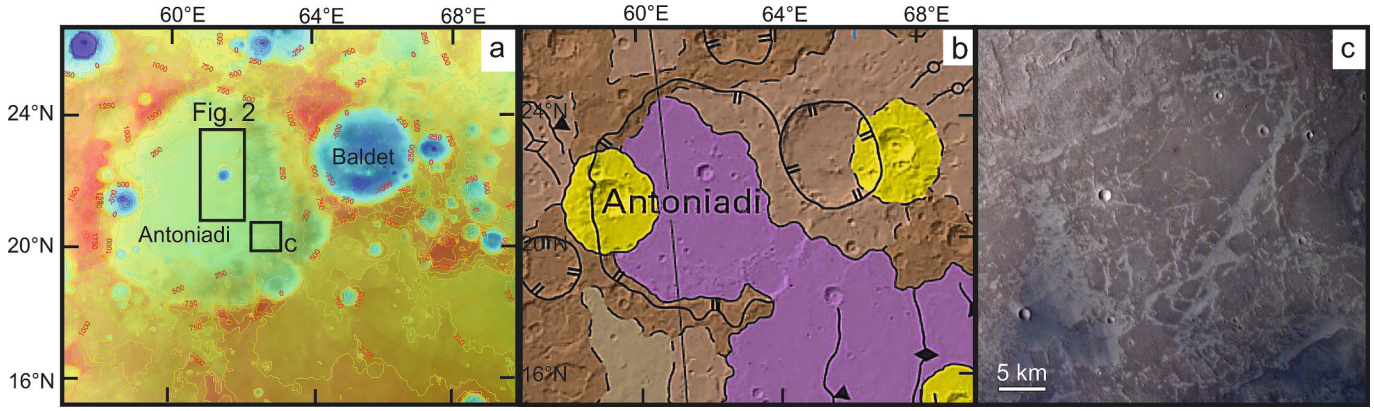

Fig. 1. Regional context of Antoniadi Basin. (a) MOLA topography in color and contours mapped over Mars Orbiter Camera wide-angle mosaic. (b) Close-up on the geological map by Tanaka et al. (2014). (c) HRSC image (#H7382_0000) over SW Antoniadi basin showing volcanic terrains with a platy texture (ESA/DLR/FU Berlin).

4.1.1. Impact craters and their ejecta

To the east of the study area, a relatively fresh, deep 170 km diameter impact crater named Baldet (Fig. 1a) has left some ejecta on the crater floor, but these ejecta do not reach the landforms of the study area. The 42 km-diameter crater A in the northern part of the study area has been filled nearly to the top of its rim (Fig. 2). Assuming a crater has a diameter D, we can estimate its initial mean depth d using eq. (1): $d = 0.323\ D^{0.538}$ for complex craters from 7 to 150 km in diameter (Tornabene et al., 2018b). The result gives an initial depth for this crater of ~2.4 km. Thus, 2 to 3 km of material has filled this crater after its formation (Fig. 2). The ejecta of crater A are mostly buried as well, except for few remnants along the outer rim (in yellow on the map Fig. 2b).

South of crater A and north of the branched ridges, crater B, a 28-km crater, appears to be better preserved than crater A (Fig. 2). The empirical depth estimation from eq. (1) gives ~1.9 km for its initial mean depth, which is consistent with the current topography. Indeed, the elevation difference from the rim to the crater center is of ~2 km, and there is no obvious filling in its center. These observations indicate that the crater B interior is pristine. The crater's inner rim is also fresh and only affected by mass wasting as observed in complex impact craters (e.g., Melosh, 1989). The crater walls do not display any fluvial or glacial landforms.

The ejecta of crater B are partly preserved on its eastern side, blanketing the surrounding plains to a radial distance of ~15 km (Fig. 2b). However, the outer blanket of ejecta is not visible because smooth plains embay the ejecta in several locations. This is apparent because the ejecta have a rough, hilly surface with radial lineations, and so plains material covers the ejecta where they are low standing, while high standing ejecta are preserved. The contact between the units is typical of embayment of the ejecta, preserving the protruding radial patterns in several locations as well as isolated hills of ejecta, i.e. like *kipuka* on Earth (Fig. 4a-b). Ejecta are much less preserved or absent along the northern, western and southern sides of crater B. There, ejecta are observed immediately along the rim and locally as irregular patches of ejecta away from the crater rim. For instance, the CaSSIS image (Fig. 4c) along the southern rim of crater B shows the presence of few hills south of the crater rim with the same texture and patterns as the ejecta on the eastern side. These hills likely correspond to buttes from ejecta otherwise buried below flat, smooth plains. Thus, smooth plain materials have filled part of the rim and most of the interior of crater A, but also a large part of the ejecta and rim of crater B without contributing to infilling its interior, which is also supported by the absence of breaches in crater B's rim.

4.1.2. Plain units

The smooth plains appear very flat; ranging from ~20 m to ~180 m

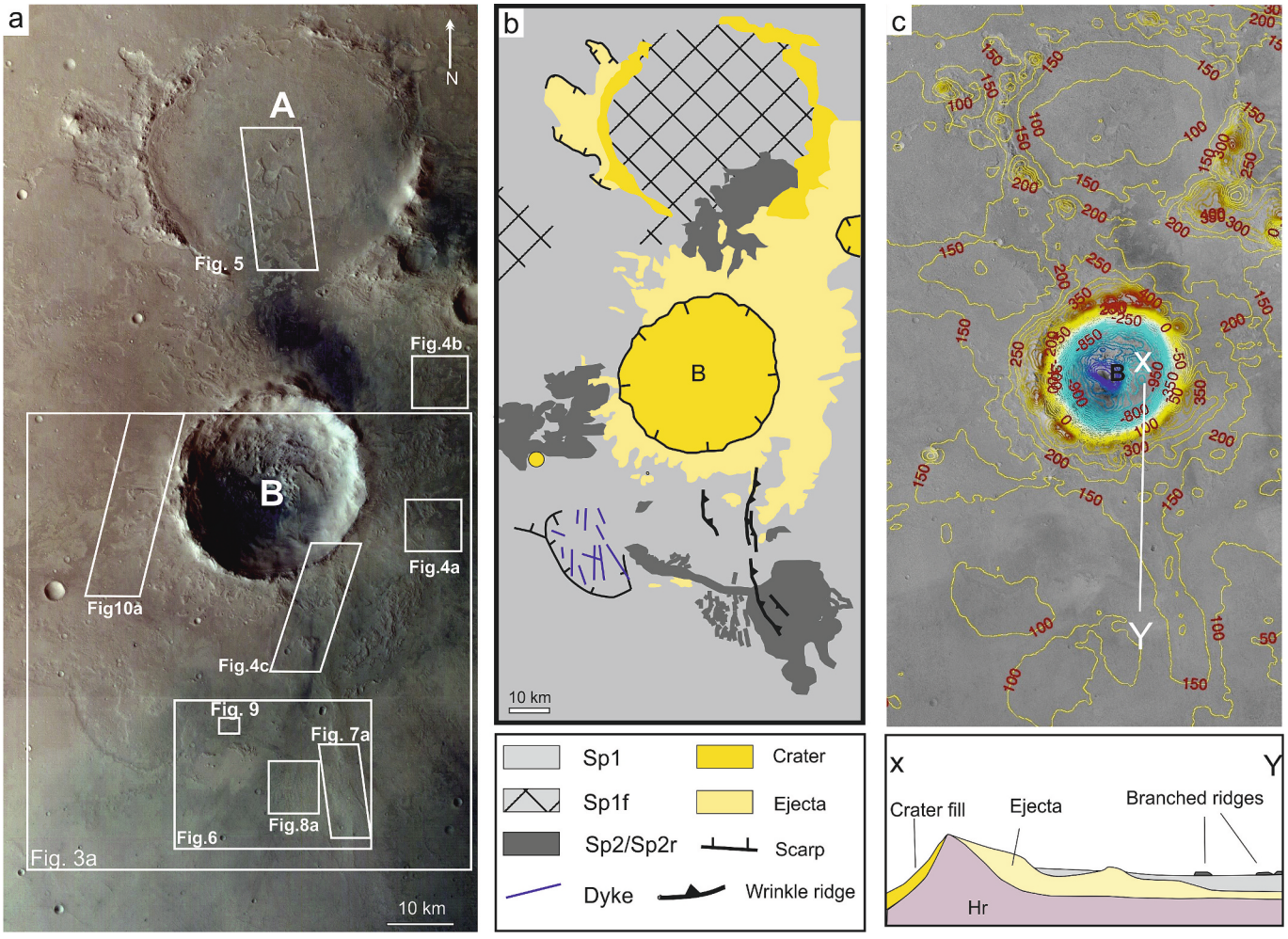

Fig. 2. Central part of Antoniadi Basin. (a) HRSC image (#H7357_0000) showing the region of interest with two impact craters A and B (ESA/DLR/FU Berlin). (b) Context map of the main units and landforms observed in the central Antoniadi Basin (NASA/JPL/MSSS/The Murray Lab). (c) MOLA topographic contours mapped over CTX mosaic. The XY cross-section is interpreted from the topography and the geomorphic observations described in the section 4. Hr: Hesperian ridged plains. Sp1: Light- and medium-toned smooth plains. Sp2: Dark-toned smooth plains. Sp1f: Same plains with flow patterns. Sp2r: Dark-toned branched ridges within Sp2 plains.

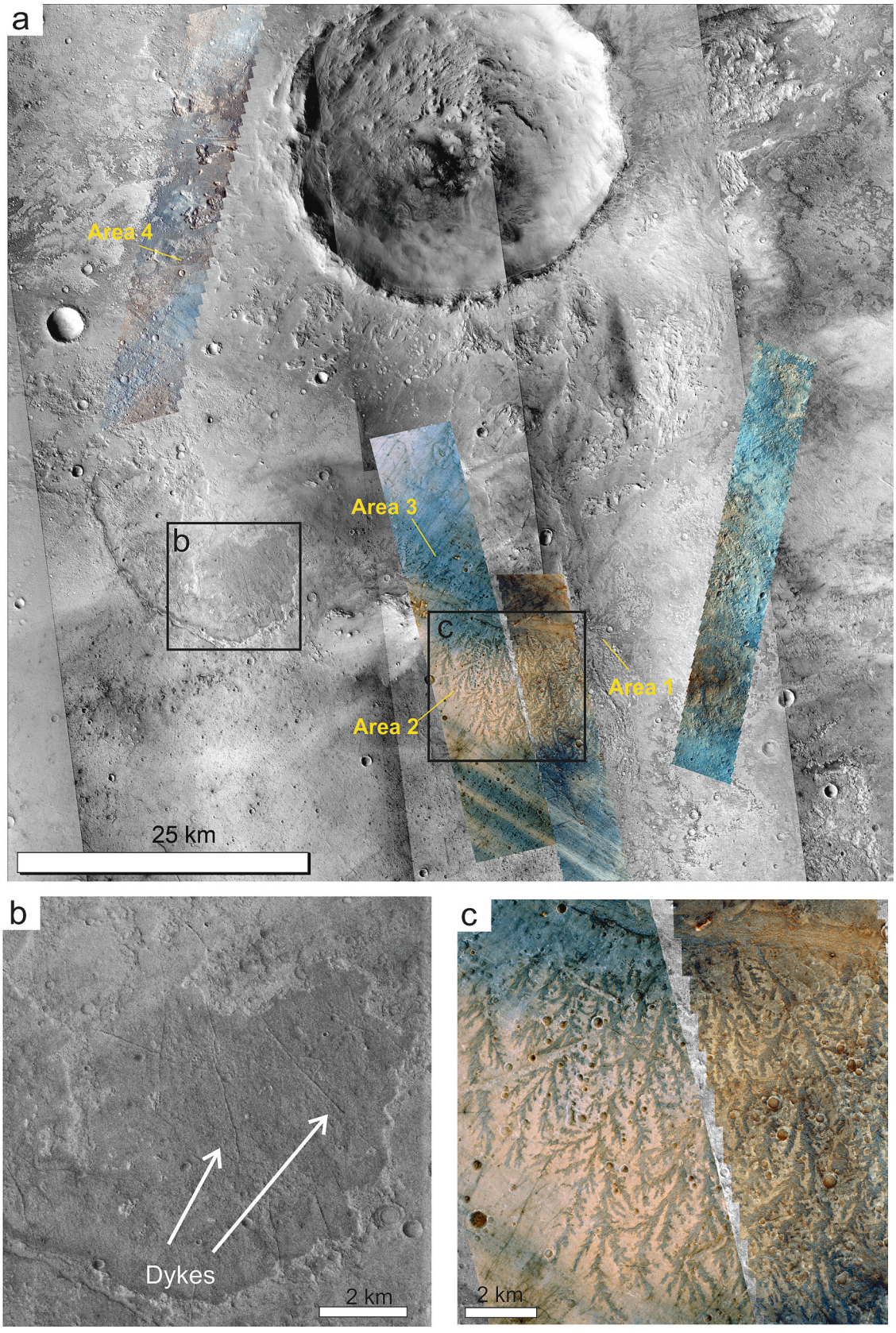

Fig. 3. (a) Four CaSSIS NIR-PAN-BLU RGB composite images overlain on CTX mosaic in the region with branched ridges. CaSSIS image numbers, from left to right: MY35_009924_025, MY36_014986_159, MY35_13494_159, MY36_016771_020 (ESA/TGO/CaSSIS CC BY-SA 3.0 IGO). (b) Close-up of the CTX mosaic on linear ridges, potentially volcanic dikes. (c) Close-up on the two CaSSIS images with dark-toned, branched ridges lying on light-toned plains.

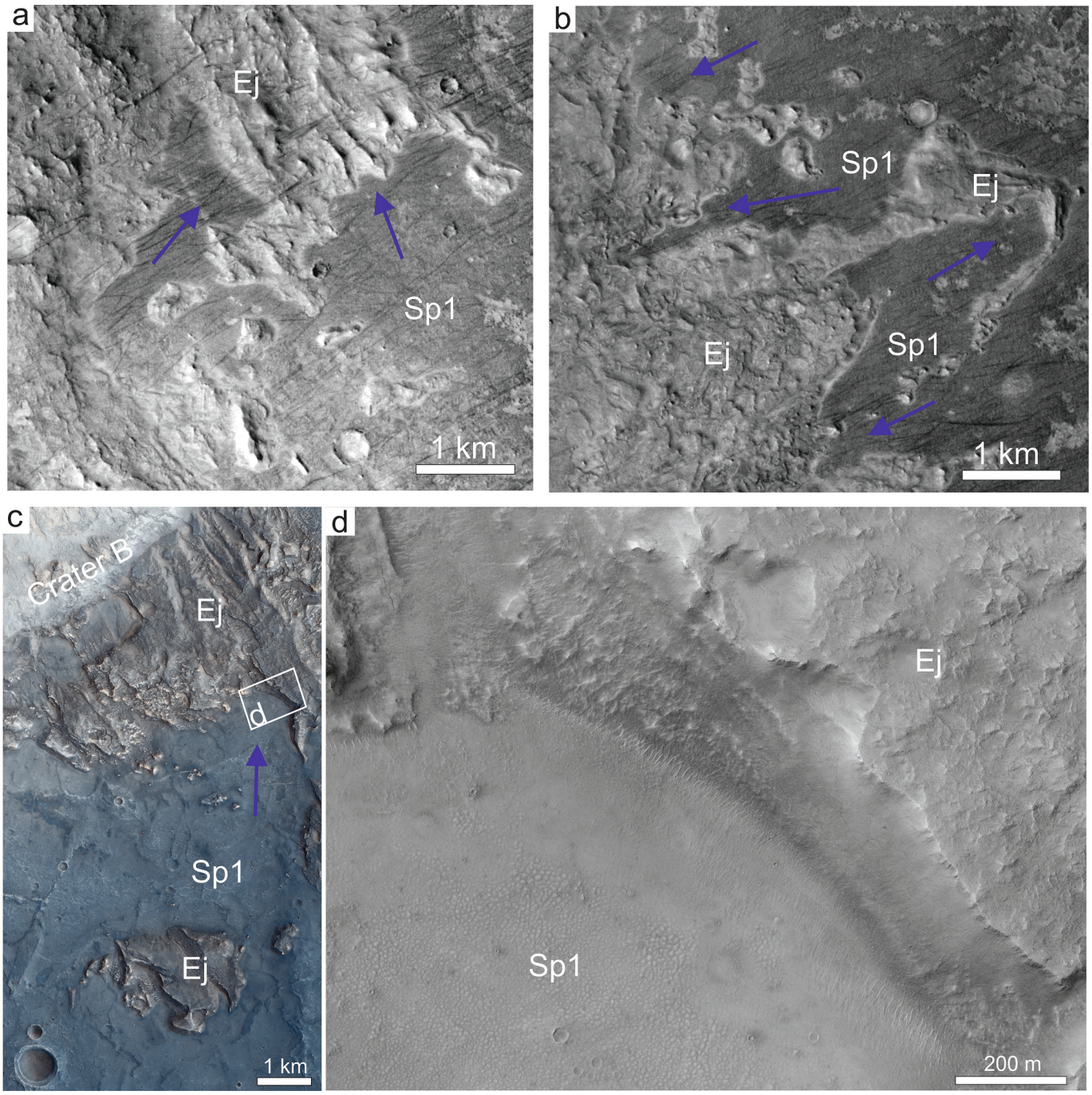

Fig. 4. Contact between ejecta and plains east and south of crater B. (a) and (b) CTX mosaic close-ups of the contact between smooth plains (Sp1) and ejecta (Ej) showing embayment of the ejecta by the plain material. Dark blue arrows indicate location where plain material onlaps the ejecta, locally leading to isolated hills of ejecta (kipuka-like hills). (c) CaSSIS NIR-PAN-BLU composite image (#MY35_010430_024) showing crater B rim and ejecta partly buried by a smooth plain material (ESA/TGO/CaSSIS CC BY-SA 3.0 IGO) showing the same embayment of ejecta by smooth plains and the isolated hills. (d) HiRISE image (#ESP_054684_2020) close up showing the contact between plains and ejecta (NASA/JPL/University of Arizona). (For interpretation of the references to color in this figure legend, the reader is referred to the web version of this article.)

of elevation above the datum (Fig. 2c). These gentle plains display an overall light- to medium-tone in HRSC images, with locally darker units (Figs. 3-7). We first focus on the light- to medium-tone plains mapped as unit Sp1 (Fig. 2). Sp1 plains display widespread patterns of polygonal fractures at the 10 m scale in all high-resolution images (Fig. 4d, Fig. 5). In places, large-scale (km-wide) sinuous landforms appear as high-standing (Fig. 5). The same polygonal networks observed on Sp1 can be observed on these sinuous features where HiRISE images are available (Fig. 5b-d), suggesting they are part of the same material. These sinuous features are present west of the study area and within crater A (Fig. 2b). Within crater A there are elongated plates of platy, blocky material at a 100 m scale that are assembled along parallel orientations tracing sinuous patterns in plan view (Fig. 5a-b). When observed at the HiRISE scale (Fig. 5b), the blocky structure displays a rough texture whereas the material between plates is smoother and has polygonal patterns of fractures at the 10 m scale. No distinct boundary between these various patterns and smooth plains Sp1 is observed. We define as Sp1f, the plains that display sinuous and/or platy features, locally

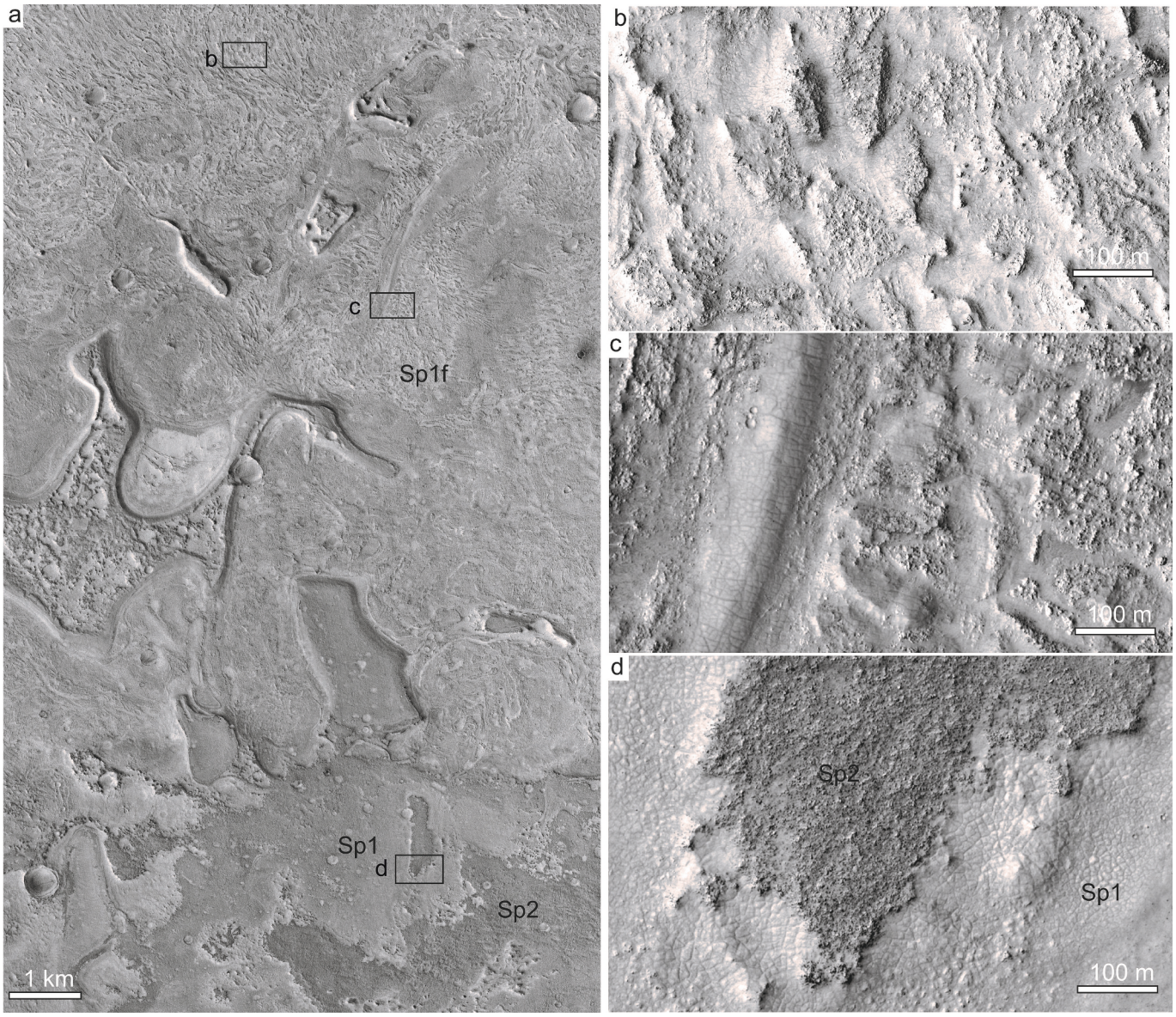

Fig. 5. (a) Close-up within crater A in the northern part of the studied region (HiRISE image ESP_ 28486_2035). (b) Close-up on the platy flows with polygonal blocks surrounded by smoother material. (c) Close-up on an arcuate ridge with same texture of material (polygonal fractures and local blocky plates). (d) Location south of crater A with plain material Sp1 with typical, polygonal fracturing overlain by Sp2 plain material type with dark tone and rubbly texture (HiRISE image PSP_8677_2035).

displaying rougher, flow-like patterns, but are continuous with the smoother Sp1 plain unit (Fig. 2b).

A second plains unit displays darker tones and rougher texture at 10 m scale. It is present in the north, west and south of crater B (Fig. 2b, S1d, 5–10). This unit is named Sp2 as it is distinct from Sp1 material based on both texture and albedo. In all locations where HiRISE is available, the surface of the dark-toned unit Sp2 reveals a rough texture and numerous boulders, but without any apparent inner structure such as layers or lineations. Locally, specific features such as branched ridges and lobes display the same texture and tone than the dark unit Sp2 (Fig. 5-10). The dark-toned unit containing branched ridges is named Sp2r hereafter (r for ridges), and on the context map (Fig. 2b). Spr2 is present mainly in the south and west of crater B. When present, Sp2 and Sp2r are always stratigraphically above Sp1. The boundary between Sp1 and Sp2 is difficult to determine where the dark-toned Sp2 is etched by wind and only partly preserved, so the map at HRSC scale (Fig. 2b) only displays Sp2 where identified without ambiguity.

4.1.3. *Tectonic structures*

The crater floor exhibits a number of elongated, shallow relief landforms (100 m high at maximum), which include wrinkle ridges (Fig. 2), similar to those commonly observed inside many plains on Mars (Watters, 1993). Wrinkle ridges are surface expressions of compressional tectonic structures often associated with volcanic plains (e.g., Plescia and Golombek, 1986) including Syrtis Major Planum (e.g., Hiesinger and Head III, 2004). Wrinkle ridges postdate the Sp1 plains in which they form, while their relationship with Sp2/Sp2r units is less obvious due to the discontinuous nature of these units.

Thin, straight ridges are also present in several locations (Figs. 2, 3, 6). These ridges are tens of meters wide, several kilometers long, and display only angular junctions (Fig. 3b), suggesting a tectonic or volcanic origin (e.g., dikes). We will refer to them as straight ridges in contrast to the wrinkle ridges and the networks of branched ridges described below.

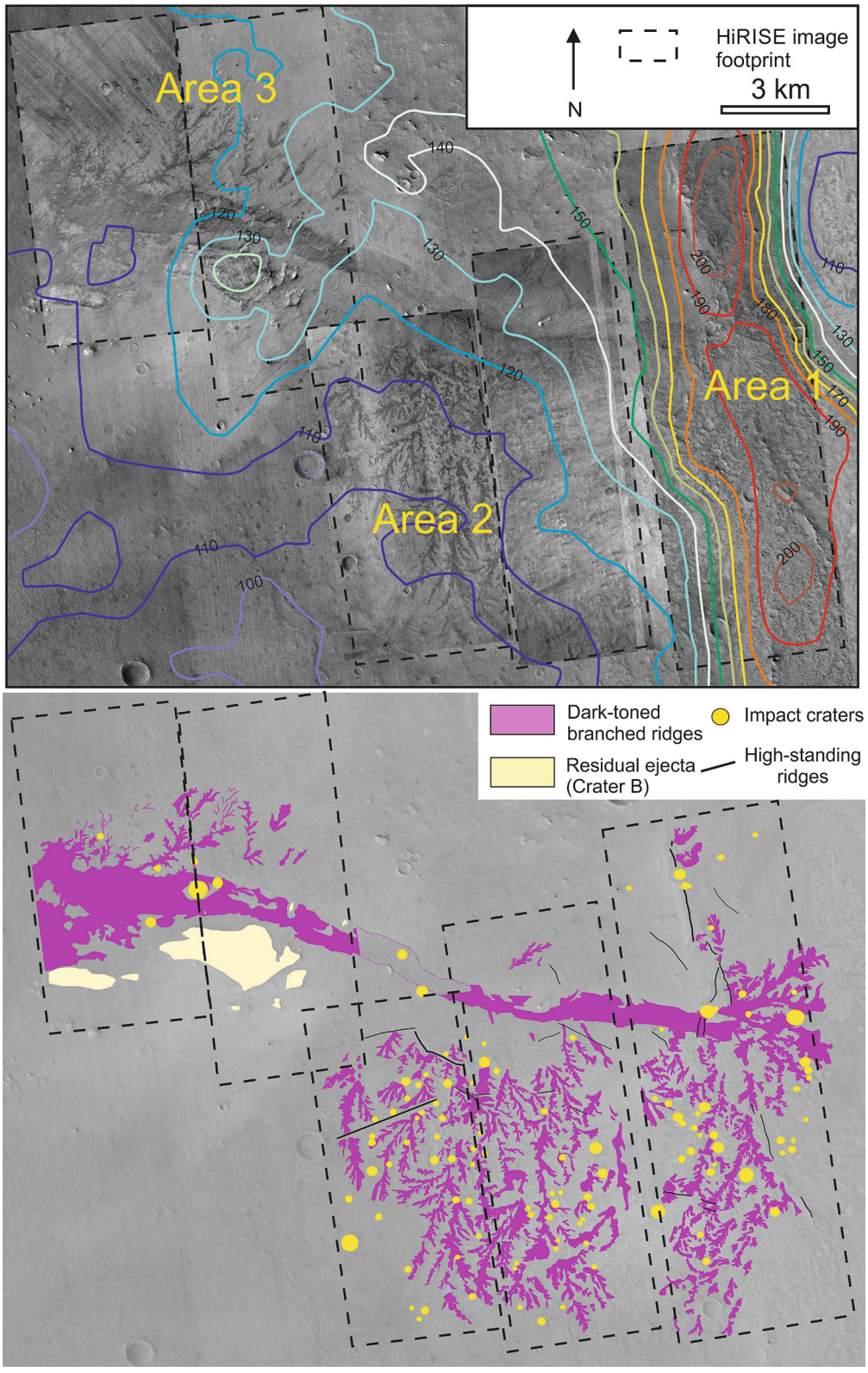

Fig. 6. (a) Close-up on the region studied with HiRISE data mapped over CTX mosaic and MOLA 10 m topographic contours. HiRISE images from left to right: PSP_007095_2020, ESP_034311_2020, ESP_057678_2015, PSP_001992_2015, ESP_013147_2015 (NASA/JPL/University of Arizona). Areas 1 to 3 are the three areas with branched ridges as explained in the text. (b) Map of branched ridges in areas 1 to 3 at HiRISE image scale (with CTX mosaic as background). Networks of branched ridges point toward a large 500 m wide ridge cross the terrain with an *E*-W direction. Residual ejecta (light yellow) are hills interpreted from their texture as initially part of ejecta of crater B before their burial by smooth plains. (For interpretation of the references to color in this figure legend, the reader is referred to the web version of this article.)

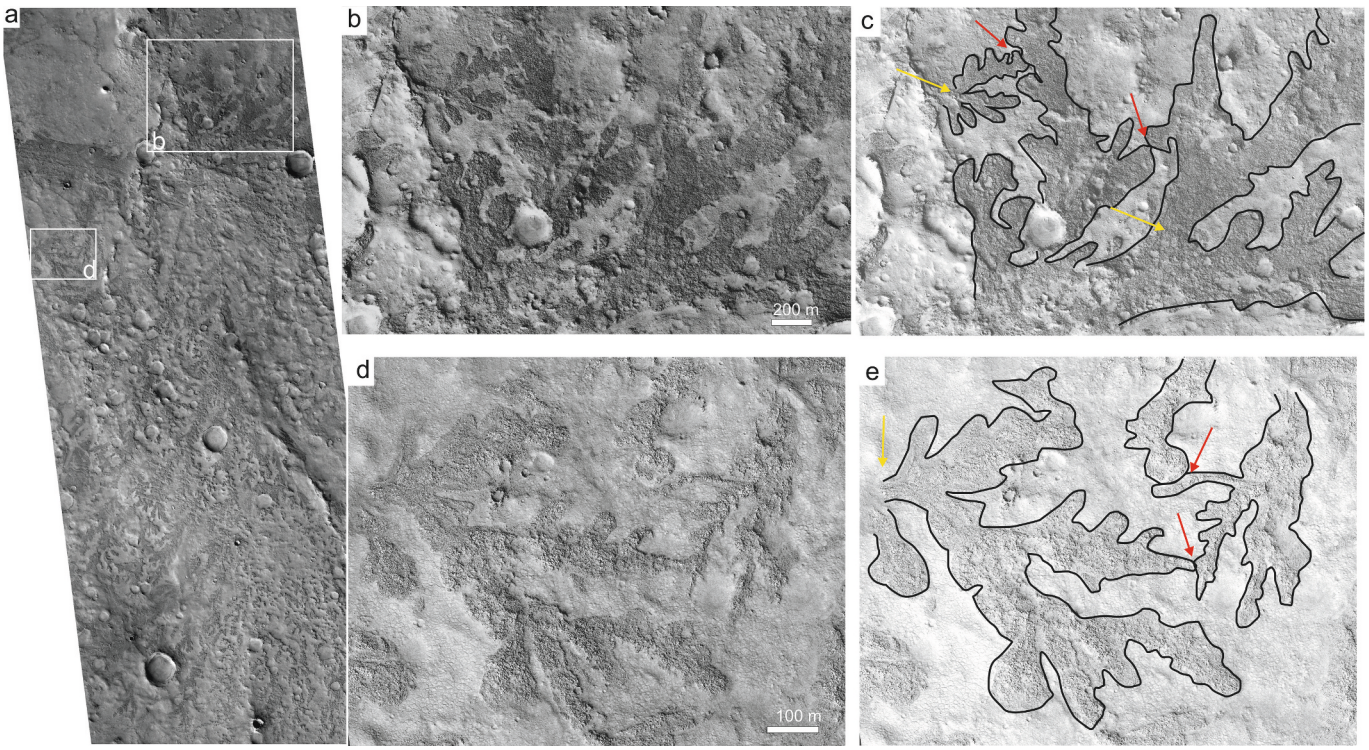

Fig. 7. (a) Networks of branched ridges in the area 1, east of the study location (close ups on HiRISE image ESP_013147_2015) (NASA/JPL/University of Arizona). (b to e) Close-ups and corresponding interpretations showing ridges with lobate shapes. Red arrows indicate locations where branches of distinct networks or sub-networks are in contact. Yellow arrows indicate locations with a narrow branch at the base of networks. (For interpretation of the references to color in this figure legend, the reader is referred to the web version of this article.)

4.2. Detailed morphology of the branched ridges

4.2.1. Qualitative observations

Four areas display variably well-developed networks of branched ridges south and west of crater B (unit Sp2r, Figs. 2-3, 6). The most spectacular branched ridges are those present in areas 1 to 3 south of the crater B (Figs. 6-9). There, an East-West trending, ~20 km long, 0.5 to 1 km wide ridge is present with the same dark tone and texture as unit Sp2 (Fig. 6). This *E*-W ridge seems to forms a backbone with several ridges branching from it to the south (area 2) and north (area 3) while area 1 is mainly toward east of this E-W oriented ridge (Figs. 6, 7).

Area 1 displays branched features covering an area of 5 by 10 km (Figs. 7a-c). These ridges are tens of meters in width and several hundreds of meters long. In the northern part of this location, ridges display lobate shapes and widths reaching locally 300 m (Figs. 6, 7b-c). A straight ridge is present on the western boundary of these lobate features. A similar set of branched, lobate ridges is observed southward (Fig. 7d). In both areas (Figs. 7b-e), branched ridges are locally in contact with each other (red arrows) and narrow at the base of each branch (yellow arrows).

The largest field of branched ridges (area 2) is 10 by 10 km across located south of the E-W trending ridge (Figs. 2, 6, 8). These branched ridges are always superimposed on the light- to medium-tone substratum crossed by a network of polygonal fractures typical of Sp1 unit. Here too, branched ridges are tens of meters in width and hundreds of meters to a few kilometers in length. They also display a dark-tone and a rubbly texture at high resolution. Detailed inspection of these landforms reveals that the edges of a few ridges are in contact with other ridges (e.g., in Fig. 8b, red arrows). The edges of some ridges display more resistant material such as levees (white arrows in Fig. 8c) and relatively lobate shapes (Fig. 8e). Several ridges present a narrowing along their path (yellow arrows in Figs. 8a, d). For instance, in Fig. 8d, we observe six minor branches (r1 to r6) connected to one trunk, which is often narrower than most of the branches.

Area 3 is 3 by 6 km across at the western edge of this region (Fig. 6). These branched ridges are located north of the central *E*-W trending ridge (Fig. 9). They are in lower number than in areas 1 and 2. These branched ridges appear to have undergone more erosion as deduced from local gaps between residual hills elongated in the same direction (green arrows on Fig. 9). Fig. 9 also shows that the E-W trending ridge (at the bottom of the close-up) has the same texture as the branched ridges, and that the latter are connected to the former.

Lastly, area 4 is an area 2 by 4 km located west of crater B (Fig. 1) that has a dense pattern of branched ridges (Fig. 10a-b). Despite being disconnected from the other areas, the branched ridges in area 4 have similar shapes, being tens of meters wide and hundreds of meters long (Fig. 10c-e). Here too, ridges are superimposed on a lighter-toned terrain with same polygonal texture typical of the Sp1 unit (Fig. 10e). These ridges are densely packed to the point that they are frequently in contact (red arrows in Fig. 10d). In addition, two ridges appear deflected by the presence of another ridge (orange arrows in Fig. 10d). Further north in the same area, the terrain displays a platy texture with individual plates of hundreds of meters wide separated by shallow trough several tens of meters wide (Fig. 10f).

In summary, there are multiple, common characteristics displayed by the branched ridges in the four areas studied: a width of several tens of meters, a length of several 100 s of meters to several kilometers, a dark tone and a rough, rubbly surface texture with submeter-size blocks. No layering or internal fabric has been identified. The presence of a narrowing along the path of main tributaries of most networks is frequent (yellow arrows in Figs. 7c, e, 8a, d, 9). Contacts between the edges of the branched ridges (red arrows) seems to be relatively infrequent where the ridges are eroded (Fig. 9) compared to locations where the ridges are dense and well-preserved from erosion (Figs. 7b-e, 10c-d). Lastly, a common characteristic of all the branched ridges in areas 1 to 3 is that they seem to be connected to the 500 m wide, *E*-W trending ridge.

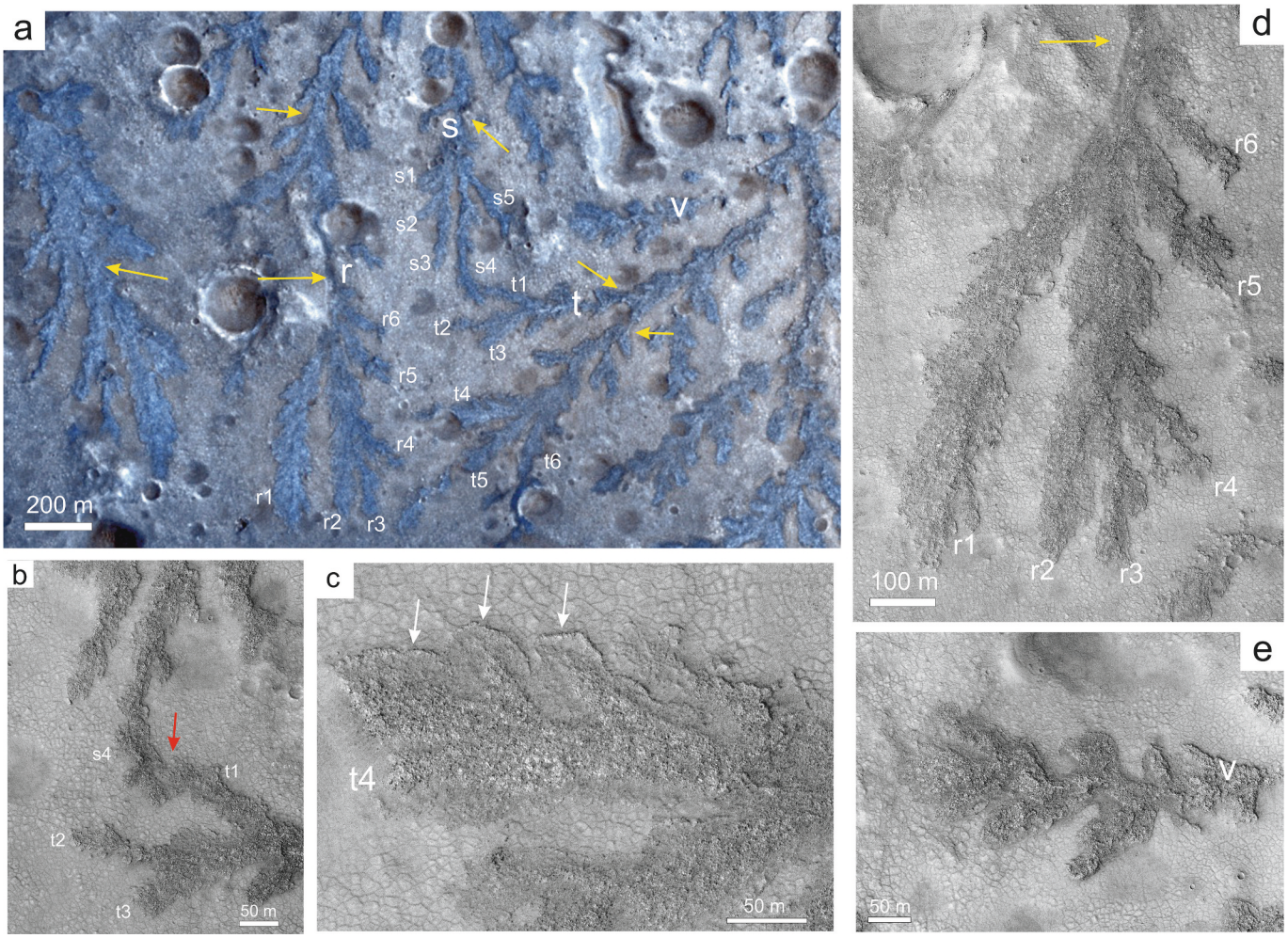

Fig. 8. (a) Close-ups on area 2 with CaSSIS (#MY35_010430_024, NIR-PAN-BLU filters) containing networks of branched ridges named r, s, t and v (ESA/TGO/CaSSIS CC BY-SA 3.0 IGO). (b to e) Close-ups on HiRISE (ESP_057678_2015) images (NASA/JPL/University of Arizona). Red and yellow arrows same as in Fig. 6. White arrows indicate lobate and high standing boundaries. (For interpretation of the references to color in this figure legend, the reader is referred to the web version of this article.)

4.2.2. *Quantitative observations*

Branched ridges can be studied using the classical network approach of either Shreve or Strahler orders used for river networks (Strahler, 1952). The Strahler method uses the number 1 for the smallest branches close to the head of the river, and each junction increases the order by 1 until reaching the outlet (Fig. 11). This method is adapted to tributary channels, but can be used for distributary channels, with the lowest number corresponding instead to the terminal branch instead of the channel head.

The pattern of the most dendritic, branched ridges in area 2 (Figs. 2 and 8) exhibits a Strahler order of 5. Junctions of small branches that form larger trunks indicate a general organization toward north, assuming that the ridges are tributaries. Yet, the main regional slope at this location is of 0.3° toward the south (Fig. 12), thus in the opposite direction to that expected if the ridges were organized as tributaries. This means either (i) that the terrain was tilted in the exactly opposite direction to the flow after the branched ridges formed, or (ii) that the ridges are distributaries, thus formed by flows dividing into branches rather than branches connecting downstream. In the case (ii), the main slope direction toward the south is consistent with their geometry without requiring an additional regional tilt.

Angles between branches were derived from the measurement of 77 angles in the area 2 that contains the highest density of branches. These measurements correspond to junction angles assuming a tributary network, or bifurcation angles assuming a distributary network. The values are distributed from 5° to 85° with a median at 47.5° ±19° (Fig. 13). Lastly, the thickness of branched ridges was measured orthogonally to branches using the HiRISE DEM (Fig. 12). Thicknesses of individual branches never exceed 4 m, without showing any geographical differences either along increasing Strahler orders or toward the north.

4.3. *Color and physical properties of the ridges*

4.3.1. *Thermal imagery*

THEMIS data provide a way to estimate the relative thermal inertia of the material in the first centimeters of the surface, which is related to the relative strength of geological units (which can mean either their lithology or various degrees of cementation), or their burial below sand and dust mantling (Christensen et al., 2004). Although the thermal inertia signal interpretation is not unique, it can still help to further refine the differences between the units identified in visible images. In nighttime THEMIS data (Fig. 14a), both the branched ridges and the *E*-W-trending ridge are lighter, thus warmer, than the smooth plains surrounding the branched ridges. This difference means that the branched ridges are made of a material more capable of retaining heat, which is often inferred to mean more cohesive materials, loosing heat more slowly compared to plains where the thermal signature is more

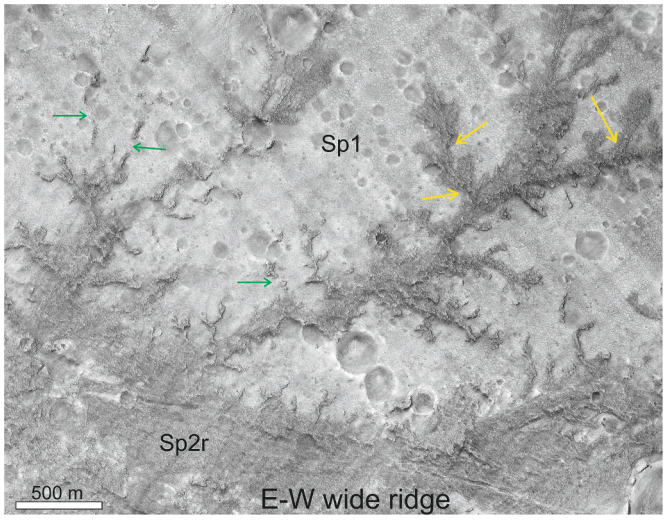

Fig. 9. HiRISE image PSP_007095_2020 showing networks of dark-toned ridges (Sp2r) superimposed on light-toned plains (Sp1) in area 3 (NASA/JPL/University of Arizona). Yellow arrows same as in Fig. 6. Green arrows show location with erosion of branches showing that ridges are more eroded than in areas 1 and 2. The branched ridges are connected to the wider E-W trending ridge that displays similar rubbly texture at <10 m scale. (For interpretation of the references to color in this figure legend, the reader is referred to the web version of this article.)

consistent with material that exchanges heat with the atmosphere more rapidly. This is in agreement with the rubbly surface of cohesive blocks on the ridges as compared to that of the plains, which are smooth at the resolution of HiRISE data, although we cannot fully rule out that their elevated inertia may be attributed to less dust cover or cementation/induration relative to their surroundings. This conclusion is consistent with the THEMIS daytime data (Fig. 14b) in which the ridges are darker, thus colder than the smooth plains that may be more dusty/less rocky in the first centimeters than the branched ridges. Thermal inertia has been computed from THEMIS data (Fergason et al., 2006) (Fig. 14c). Although many branched ridges are too narrow to be clearly visible at the scale of this map (100 m/pixel), values on the largest ridges, such as the E-W wide ridge scatter from 350 to 500 tiu (thermal inertia unit) compared to100–200 tiu for the underlying plains. Such values are in agreement with the qualitative assessment that the branching ridges are composed of relatively dust-free, rocky material.

4.3.2. *CaSSIS spectral channels*

We have performed a spectral analysis of the branched ridges and light-toned terrains using the available filters (3–4 filter combinations are possible) of the CaSSIS data that currently covers the site. There is one CRISM cube covering part of the area 2 containing branched ridges, but we do not present it because the corresponding spectra are dominated by dust at the CRISM spatial scale and do not enable us clear mineralogical identification beyond what has been done using CaSSIS data.

The branched ridges appear as a distinct dark blue in all CaSSIS NIR-PAN-BLU (NPB) color-infrared images with slight variations toward lighter colors that may be related to local dust-cover. A color band ratio composite (CBRC) using CASSIS NIR/PAN, PAN/BLU and PAN/NIR in R-G-B (i.e., CBRC-NPBa; Tornabene et al., 2018a) accentuate these differences (Fig. 15), which generally relate to differences in ferrous vs. ferric content. In contrast, the plains and straight ridges display lighter colors in CaSSIS NPB, and from yellow to orange in the CBRC with some green areas suggestive of mixing eroded blue and yellow components (Fig. 15).

These differences in colors can be plotted as spectra to compare with laboratory data on Earth. Of all the CaSSIS images taken over the investigation site, image MY35_010430_024_0 offers the best quality and covers the majority of the key surface features and associated local units. MY35_010430_024_0 also provides a low estimated dust opacity (~0.01) and sufficiently high incidence for shadows (~36°) required for correction and analysis through the dark object subtraction (DS) method (Tornabene et al., 2018a, 2018b), which is necessary to minimize the impact of ferric dust aerosol scattering on surface spectra. Unfortunately, this CaSSIS cube was only taken with three filters (NIR-PAN-BLU) and not all four. Despite this, we can use the three filters to make some inferences regarding the general composition and possible dust-cover with respect to the units represented in the scene. MY35_010430_024_0 DS-corrected I/F spectra of the main E-W ridge (R) and branched (Br1 and Br2) features consistently have a lower reflectance and a deflection toward 1 μm, which is usually due to the presence of unaltered ferrous component such as mafic minerals, namely pyroxene and olivine (Br1 to Br3, Fig. 15b-c). This trend is observed for the bluest portions of the E-W trending and branched ridges (extracted from various locations to test these possible variations). They also show a significant reduction in a BLU band absorption when compared to the spectral characteristics of the lighter-toned substrate, including a reduction in the PAN/BLU ratio and the overall slope from IR to blue. The CaSSIS 3-point spectra have shapes most consistent with High Calcium Pyroxene (HCP) and an Fe-rich olivine endmember (i.e., fayalite); however, without the 4th filter or knowing if a 2 μm absorption is present, it is difficult to assign a specific phase or rule out if these characteristics are due to mixing Low Calcium Pyroxene LCP or Mg-rich olivine with some ferric component. Nevertheless, these spectral characteristics are sufficient to support that the branching ridges are dominated by a mafic component when compared to its surroundings, and are likely basaltic in composition. Bluer plains of intermediate reflectance (P1 and P2) when compared to the branched ridges, display a weaker but similar deflection to higher wavelengths, also suggestive of mafic minerals.

The light-toned substratum Sp1 under the branched ridges displays consistent deflections toward the BLU band, a lack of IR deflection and higher PAN/BLU and NIR/BLU ratios (L1 to L3 on Fig. 15b-c). Such slopes may be attributed to a ferric component, e.g. hematite or ferric dust. An alteration component is possible based on the lab spectra of phyllosilicates (nontronite in Fig. 14d), but the number of bands and wavelength sensitivity range of CaSSIS makes it impossible to evaluate their presence. As before, mixing of components to explain difference in slopes and deflections is difficult to rule out, but we have sufficient information to say that these units are ferric-component dominant.

Another CaSSIS image, MY36_016771_020_0, which lies east of area 1 in Fig. 3, was taken with all 4 filters and offers a good DS correction, but only provides spectra from units Sp1 and Sp2; despite this, the DS-corrected spectra extracted from MY36_016771_020_0 for these two units shows similar spectral characteristics to the Sp1 and Sp2 spectra from 3-filter MY35_010430_024_0. The consistency between the two provides support for the previous interpretations of the MY35_010430_024_0 results.

Overall, the dark color in panchromatic images and dark blue color in color composites from CaSSIS data support the presence of mafic minerals in all the branched ridges (Sp2r unit) and the dark-toned plains unit (Sp2). Smooth plains Sp1 with intermediary tone also display signatures consistent with the presence of mafic minerals but the lighter-toned areas of Sp1 suggest a predominance of ferric component, rather than mafic mineral signature.

4.4. *Chronology*

4.4.1. *Crater count model ages*

Crater retention ages are estimated using tools developed by Michael and Neukum (2010) based on isochrons developed by Hartmann and Neukum (2001). A first crater distribution plot was done using an HRSC image on a suitably large area of 1232 km^2, which corresponds overall to

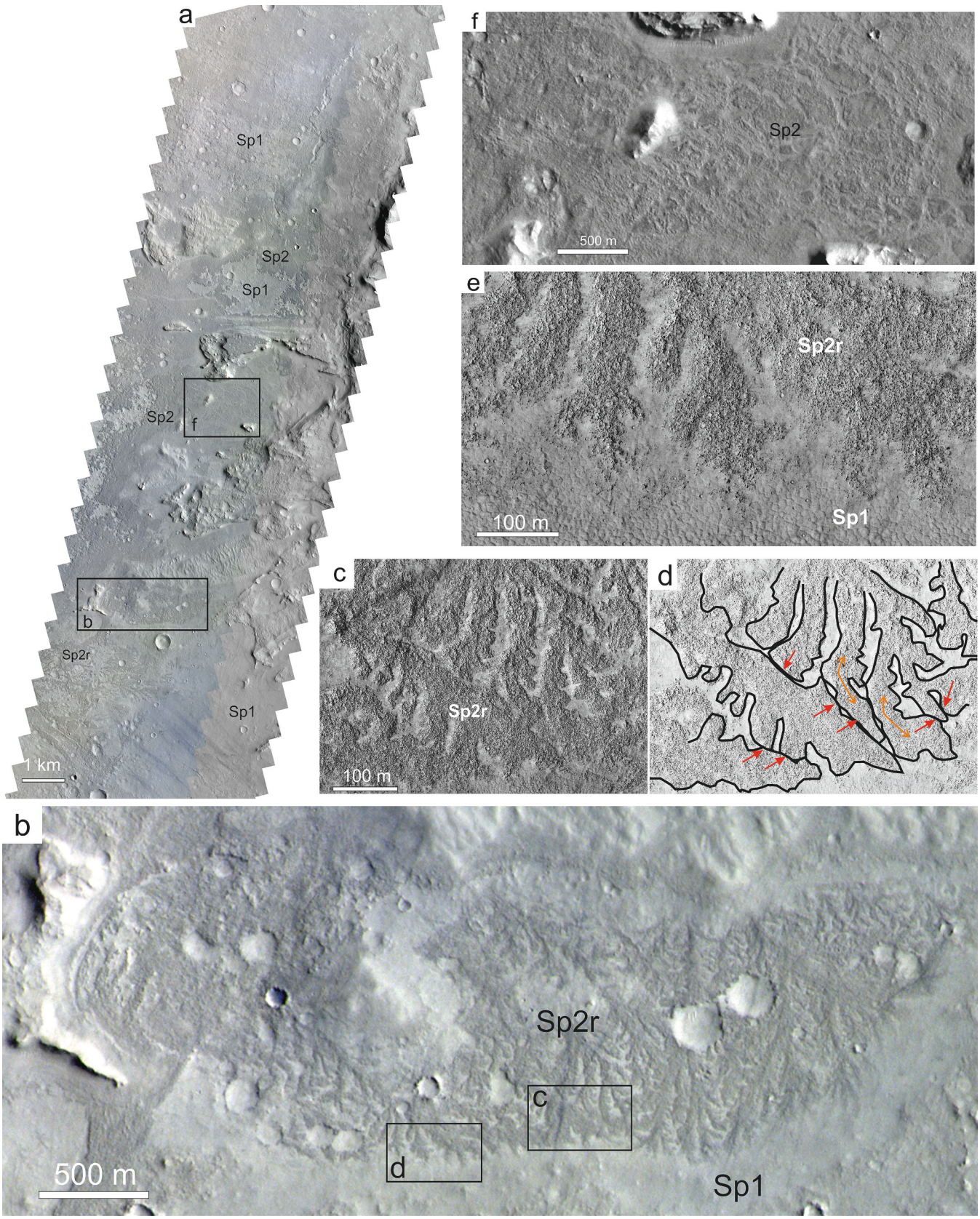

Fig. 10. (a) CaSSIS image MY35_009924_025 with NIR-PAN-BLU filters of area 4 west of crater B (ESA/TGO/CaSSIS CC BY-SA 3.0 IGO). (b) Close-up on CaSSIS image with a network of dark toned ridges sequestered in a local low. (c and e) Close-ups in HiRISE image (PSP_007240_2020) showing details of branched ridges (NASA/JPL/University of Arizona). (d) Interpretation of (c) showing ridges that are in contact to each other's (red arrows). Orange arrows indicate locations where ridges have changed their orientation after contact with other ridges. (For interpretation of the references to color in this figure legend, the reader is referred to the web version of this article.)

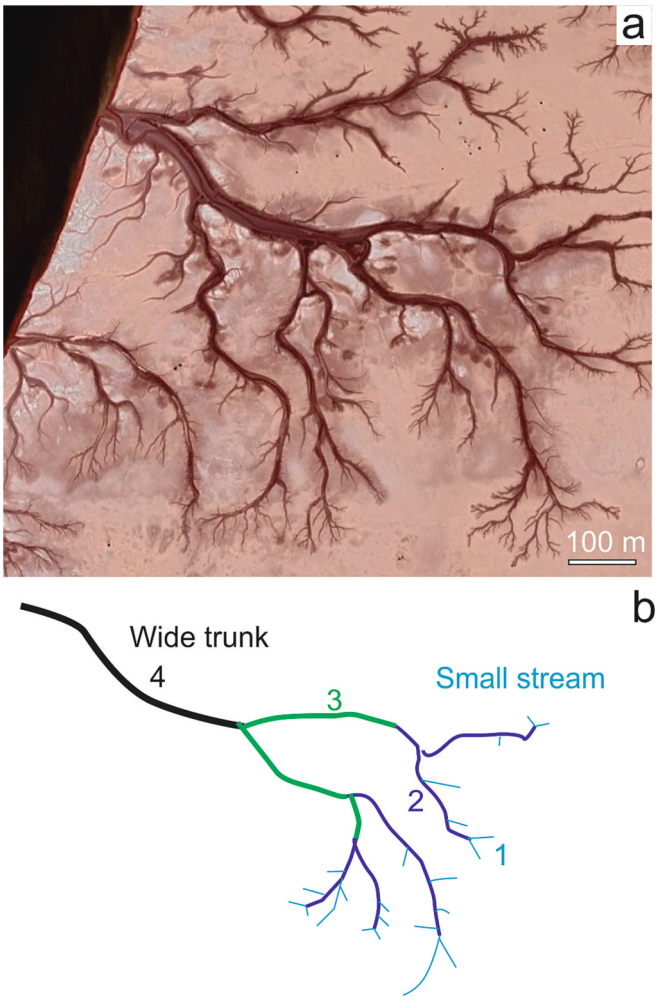

Fig. 11. (a) Image of Colorado delta on Earth showing a river network formed by seepage (Image Google Earth, Maxar technologies). (b) Sketch showing Strahler orders (Strahler, 1952).

the light-toned plains Sp1 mapped in the area of interest (Fig. 16). We have measured the diameter of 111 craters from 0.2 to 1.55 km. The downturn of the plot at <300 m seems related to the image quality, which is relatively low probably due to lightening conditions and dust. The distribution does not show any significant upturn at large diameters that could mean two phases of deposition. To be conservative, we fit the isochron with craters >400 m. The estimation made using the corresponding 38 craters gives an age of 2.56 Gy −0.41/+0.37, which corresponds to the Early Amazonian epoch (Michael and Neukum, 2010).

A second crater distribution plot is performed on a CaSSIS image on the part of the floor where the branching ridges are the most developed over a total area of 61 km^2 (Fig. 16). We have measured the diameter of 86 craters from 0.1 to 1 km. The distribution shows a downturn at low diameters (<150 m) that can be explained both by an effect of image resolution and a degradation of the surface that has erased some of the smallest craters. To be conservative, we fit the isochron with craters of 200 m and higher. The estimation made for the 23 corresponding craters gives an age of 2.49 Gy −0.51/+0.49. Taking craters larger than 150 m does not modify the result significantly.

The agreement between the two results show that the crater retention age of plains in the area of the branching ridges is of ~2.5 ± 0.5Gy, in the Early Amazonian epoch. Note that the large error bar for both plots is not only due to the relatively low number of craters used for the fit. This period of Mars' past is the most challenging for the estimation of crater counts, because the model has the largest error bars for that period (Michael and Neukum, 2010).

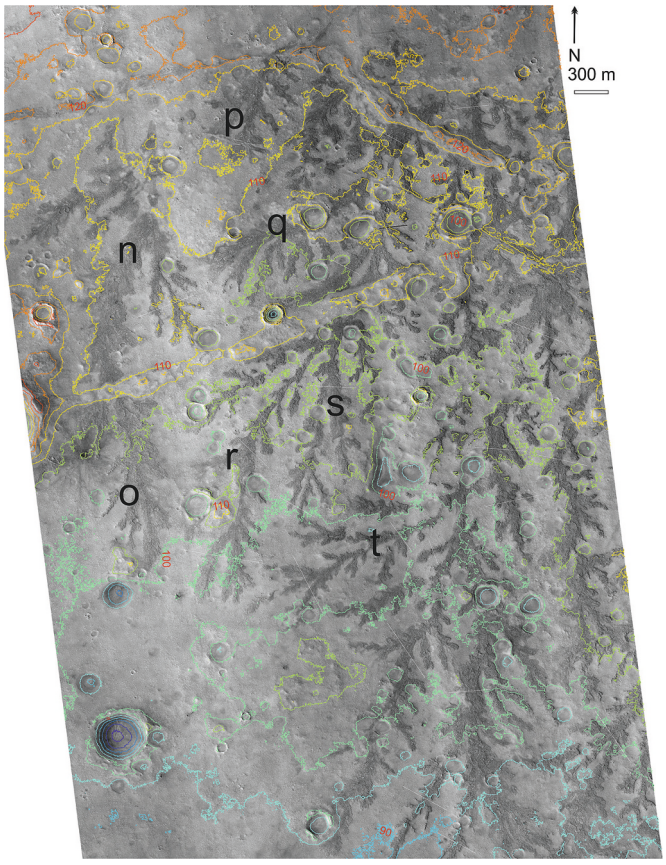

Fig. 12. HiRISE image with corresponding Digital Elevation Model made from HiRISE images ESP_057678_2015 & ESP_057546_2015) (available at www.uahirise.org/dtm/dtm.php?ID=ESP_057678_2015) (NASA/JPL/University of Arizona). Letters *n* to *t* corresponds to networks or sub-networks on which bifurcation angles have been measured.

4.4.2. *Relative stratigraphy and interpretation of the geological units*

Crosscutting relationships show that craters A and B are the oldest structures in the part of the Antoniadi basin studied. Crater A has been filled by all plain units (Sp1, Sp1f, Sp2, and Sp2r). Crater B seems to be better preserved, but the smooth plains embay or bury crater B ejecta, thus demonstrating that these plains postdate both craters A and B. If crater B was younger than these plains, we would observe these plain materials emerging under ejecta sections, rather than an embayment relationship (Fig. 4a-c). Sp1 and Sp1f seem to be in stratigraphic continuity, which we interpret as different expressions of the same unit, with local platy texture and viscous flow patterns typical of volcanic lavas (Fig. 5). The presence of polygonal fractures at a 10 m scale could be associated with other processes (desiccation, cooling, periglacial thermal contraction cracking, etc.), but similar patterns were also identified as indications of volcanic flow cooling in the South Elysium region (Ryan and Christensen, 2012). The presence of wrinkle ridges, which are landforms typically found in volcanic plains on terrestrial planets (e.g. Watters, 1993), and the flat, thick fill (~2 km) within crater A, are two observations also in agreement with such a volcanic origin. In color data, Sp1 have various tones with intermediate toned consistent with mafic minerals, but lighter tones require a ferric component in the surface material.

Sp2 and Sp2r are observed to always superpose Sp1, thus they postdate Sp1, and craters A and B as well (see cross-section in Fig. 2c). There is no evidence that any material above Sp2/Sp2r ever existed in the study area, such as residual buttes. No Sp2/Sp2r material is observed

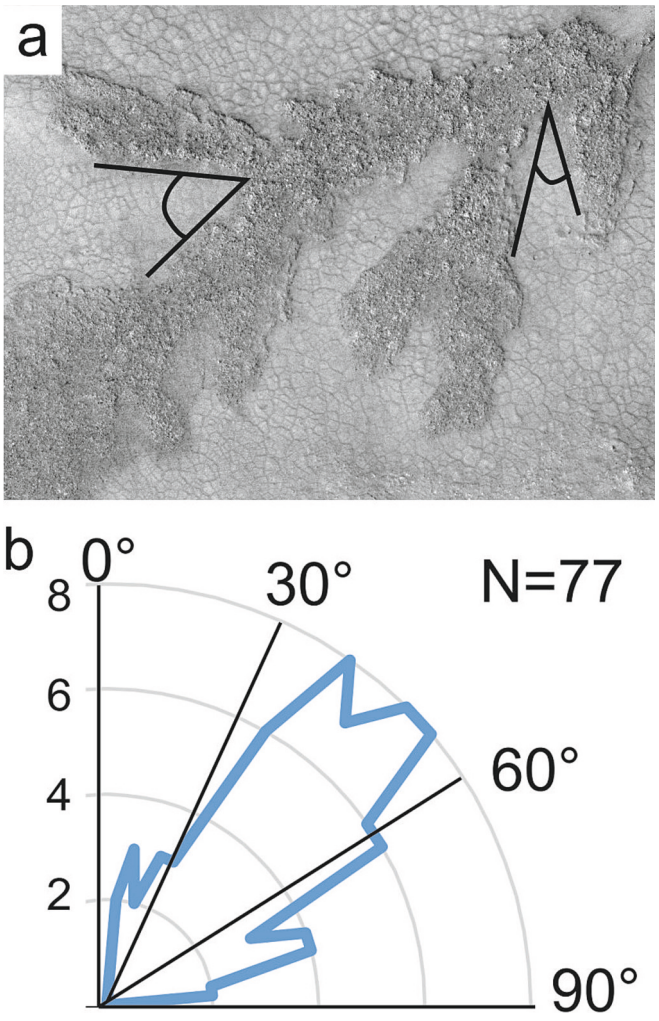

Fig. 13. (a) Close-up on junctions of two ridges showing how bifurcation angle are measured. (b) Statistical diagram with number of bifurcation angles plotted along circular lines in bins of 5°.

stratigraphically at the base of crater B ejecta either. Sp2/Sp2r is thus the uppermost type of material mapped in central Antoniadi basin. Mafic minerals explain the dark bluish color. We infer that this material is not exhumed or preserved from a thicker unit, but is rather the last episode of deposition in the center of Antoniadi basin. In addition, the observation that Sp1 plains have a ferric component, suggests either that Sp1 plains are composed of volcanic material that has been oxidized or coated by dust before the deposition of Sp2 (possibly implying a time gap), or that the Sp2r rocks display cleaner basaltic spectra because they have been etched by wind due to their higher standing position. The nature of Sp2r is discussed in section 5.1.

Craters A and B do not present any obvious evidence of fluvial or glacial landforms. Amazonian craters are generally fresh and do not exhibit fluvial erosion, while Hesperian craters display frequent incision by fluvial activity (Mangold et al., 2012), although there are a few exceptions (e.g., Mojave crater, Williams and Malin, 2008). The lack of fluvial landforms on both craters suggests that an Early Amazonian age is plausible for these craters, as suggested by their presence on basin floor, thus after the formation of the Hesperian-aged flood volcanism associated with Syrtis Major Planum regional activity (Tanaka et al., 2014; Fawdon, 2016).

Based on both crater counts and relative stratigraphy, we can summarize the age of the units as follows: (i) Craters A and B are both older than the plains Sp1, thus formed before 2.5 Ga, and just after the Hesperian flows associated with the major building phase of Syrtis Major Planum; (ii) Sp1 formed at ~2.5 Ga in the Early Amazonian from flood volcanism; (iii) The branching ridges form at ~2.5 Gy as well, or later. At this stage, the age of the branched ridges is consistent with the Early Amazonian age suggested by Zaki et al. (2020), but is contrary to De Blasio (2022) who refers to them as Noachian landforms. A Noachian age is excluded by the stratigraphy and not supported by the crater counts.

5. Discussion on the formation of the branching ridges

5.1. Tributary or distributary flows?

The branched ridges display a high spatial density and a peculiar dendritic pattern, which is the main reason that these ridges have been interpreted as fluvial landforms (Zaki et al., 2020) or dendritic precipitates (De Blasio, 2022). The most intuitive explanation would favor a formation as inverted channels from deposition of fluvial sediments by river flows, and their later preservation against erosion by inversion of relief (e.g., Zaki et al., 2021). Hereafter, we discuss the observations in favor of either tributary flows (such as rivers) of distributary flows (such as alluvial fans, lahars or lava flows) for the formation of these branched ridges.

Fluvial landforms follow empirical laws that are well determined from terrestrial studies. When several order 1 tributaries join, they form a tributary of order 2 that is usually wider, because the discharge rate of the latter is equal to the sum of the discharge rates of all order 1 streams. In all areas studied, we observe that the width of the branched ridges does not increase when increasing their order, even for orders 4 or 5; the one exception is the big *E*-W trending ridge. In some places, we observe six order 1 ridges joining to form one order 2, which appear to be narrower than the six order 1 tributaries (Fig. 8d). This narrowing along the path is observed at several locations (yellow arrows in Figs. 7-10). Differential erosion of ridges could be due to better preservation along more cemented or coarser sections, and this effect could explain the narrowing. However, one would need to explain why erosion would be more efficient for higher Strahler orders. The relatively uniform thickness and texture of branched ridges does not favor any strong difference in erosion from place to place within a given network.

Assuming order 1 tributaries are valley heads (as in fluvial flows) would also imply that these order 1 segments should be the smallest tributaries. Yet, order 1 segments are often larger than order 2 and display a lobate shape in plan view (Figs. 7-9). In addition, several order 1 segments seem to be in contact each other (red arrows on Figs. 7-8, 10). These two observations are contrary to expectations for valley heads, which to initiate require a flow coming from a source such as a spring, which are naturally separated from each other. Terrestrial examples of river flows show that order 1 flows usually do not connect together (Fig. 11a). In contrast, if the flows are distributary, then terminal deposits could display lobate shapes and could stop on other branches of the same order. It would also explain why some flows deviated from their main flow direction (orange arrows in Fig. 10). De Blasio (Fig. 16 in De Blasio, 2022) also identified locations where small topographic ridges have deviated the formation of ridges southward, and formed terminal lobes, again, unlike tributary channels.

The pattern of branched ridges does exhibit similarities to networks formed from groundwater seepage. Yet, such networks display bifurcation angles of 72° on Earth, a value obtained in a seepage network over 5000 bifurcations in 100 km^2 (e.g. Devauchelle et al., 2012), an area similar in size to the areas 2 and 3. This number of 72° corresponds to $2\pi/5$, a value that is explained by theoretical considerations (Devauchelle et al., 2012). Here, we observe bifurcation angles grouped around 47°, distinct from that of seepage networks. Bifurcation angles of the valley networks can also vary according to climate conditions (Seybold et al., 2018) or debris flows regime (Hooshyar et al., 2017). Arid regions on Earth display bifurcation angles <50° that could potentially explain the low values of branched ridges. Yet, values computed by Seybold

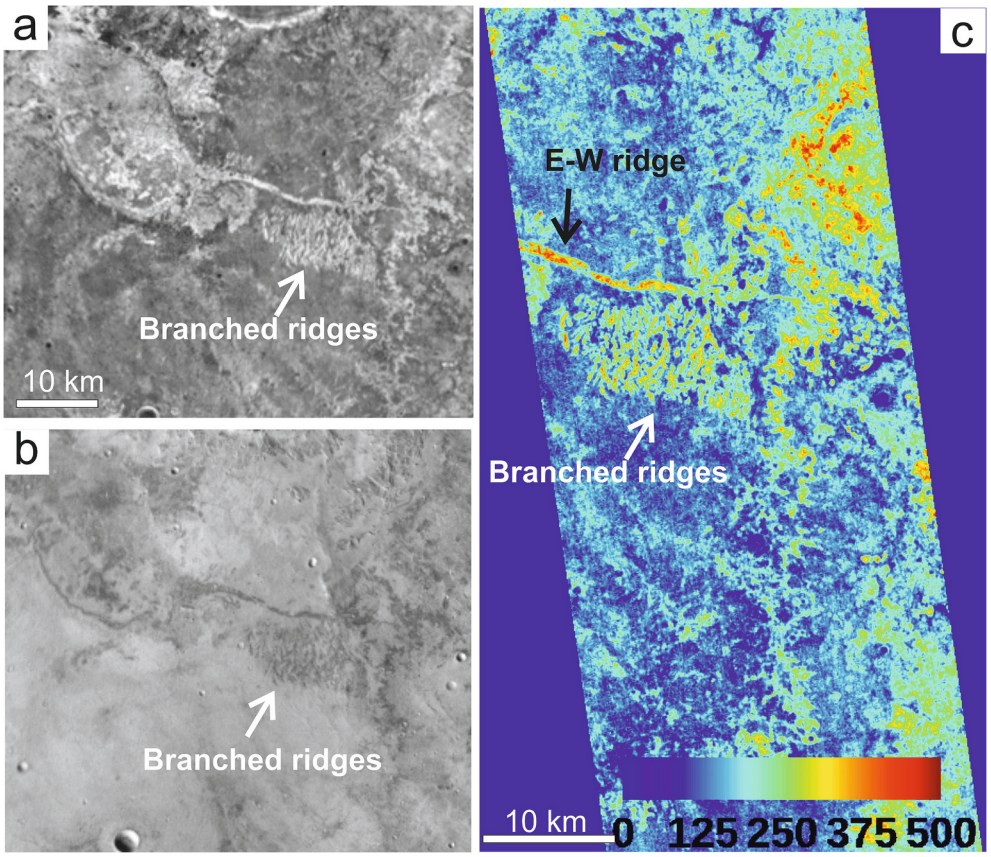

Fig. 14. (a) Night-time THEMIS mosaic showing branched ridges and the connecting E-W trending, wide ridge with a light tone consistent with relatively high thermal inertia. (b) Day-time THEMIS mosaic displaying opposite tones as expected for daily observations for which dusy/sandy material is more quickly heated. (c) Thermal inertia map of the location.

et al. (2018) represent valley systems over huge watersheds (> > 100 km^2) at a scale different from the channels studied. Moreover, in the second possibility, debris flows cannot explain the emplacement on relatively flat plains as they require steeper slopes to form and propagate (e.g., Iverson, 1997).

Taking area 2 as a reference, the current slope is oriented to the SSW by 0.3°, so it is able to explain the geometry of branched ridges only if they are distributary channels that flow in that general direction.Yet, the location south of area 1 and the wide E-W ridge do not fit the directions of current topography, suggesting a substantial modification afterward, whatever their initial process of formation. From the Fig. 7 we infer that the N-S wrinkle ridges could have uplifted the eastern region of the study area. Therefore, it is possible that some of the branched ridges have been tilted by the wrinkle ridge, and had a different initial orientation. That said, an initial orientation of the slope consistent with tributary flows would assume the main E-W wide ridge to be the location of the previous lowest point, i.e. a simple inversion of topography cannot explain why areas 2 and 3 are converging toward the wide E-W ridge. These observations also do not fit the multiple lines of evidences favoring that favor the ridge geometry being explained by viscous lobes, but suggest that they formed before the structure of the wrinkle ridge. Note also that the N-S wrinkle ridge has the same orientation as the fractures from which lobate ridges emerge in area 1, suggesting an reactivation of these structures, or a coeval evolution.

Another observation can be made when comparing the patterns from area 1 to 3 (Fig. 17). In area 1, the shape of branched ridges is relatively well-preserved from erosion, with lobate shapes and local levees. In area 3, the ridges are strongly affected by erosion, while in area 2 the erosion is moderate. We interpret that the differences in the shape of ridges is only due to differences in eolian erosion from east to west in the area studied. Indeed, these examples show that the pattern is actually very similar in all locations. For instance, Fig. 17 shows that we can reconstruct a network of branched ridges similar to that in area 1 by interpolating the assumed previous perimeter (dotted lines) around these more eroded ridges, showing that most branched ridges actually started with lobate, rounded shapes.

Overall, distributary flows can explain most observations more easily than tributary flows (Fig. 17c). In particular, it can explain that the order 1 segments are terminal lobes locally ending in contact with previous lobes. Distributary channels can form by several processes (e.g., alluvial, lahars, lava flows, etc.) that are discussed in the next section.

5.2. *Did the branched ridges form by lava flows?*

Inverted channels can form as tributary channels (such as common river flows) and as distributary channels such as in alluvial or delta fans. As discussed above, distributary channels can better explain the observed characteristics. Inverted fluvial channels are composed of sedimentary deposits, with internal bedding, deposited by river flows as sandstones or conglomerates that become more consolidated and have a higher resistance against eolian erosion than surrounding flood deposits dominated by siltstones and mudstones. They are left in relief after exhumation, but surrounding terrains usually contain residual buttes of the partly eroded, softer deposits. These characteristics are also valid on Mars (Fig. 18) (e.g., Williams et al., 2009). Yet, none of these characteristics are observed around the branched ridges located within Antoniadi basin. In addition, their rough, massive texture is distinct from other inverted channels observed on Mars. Inverted channels on Mars usually have a low thermal inertia (dark on THEMIS nighttime images, Fig. 18), while at Antoniadi basin they appear to have a higher thermal

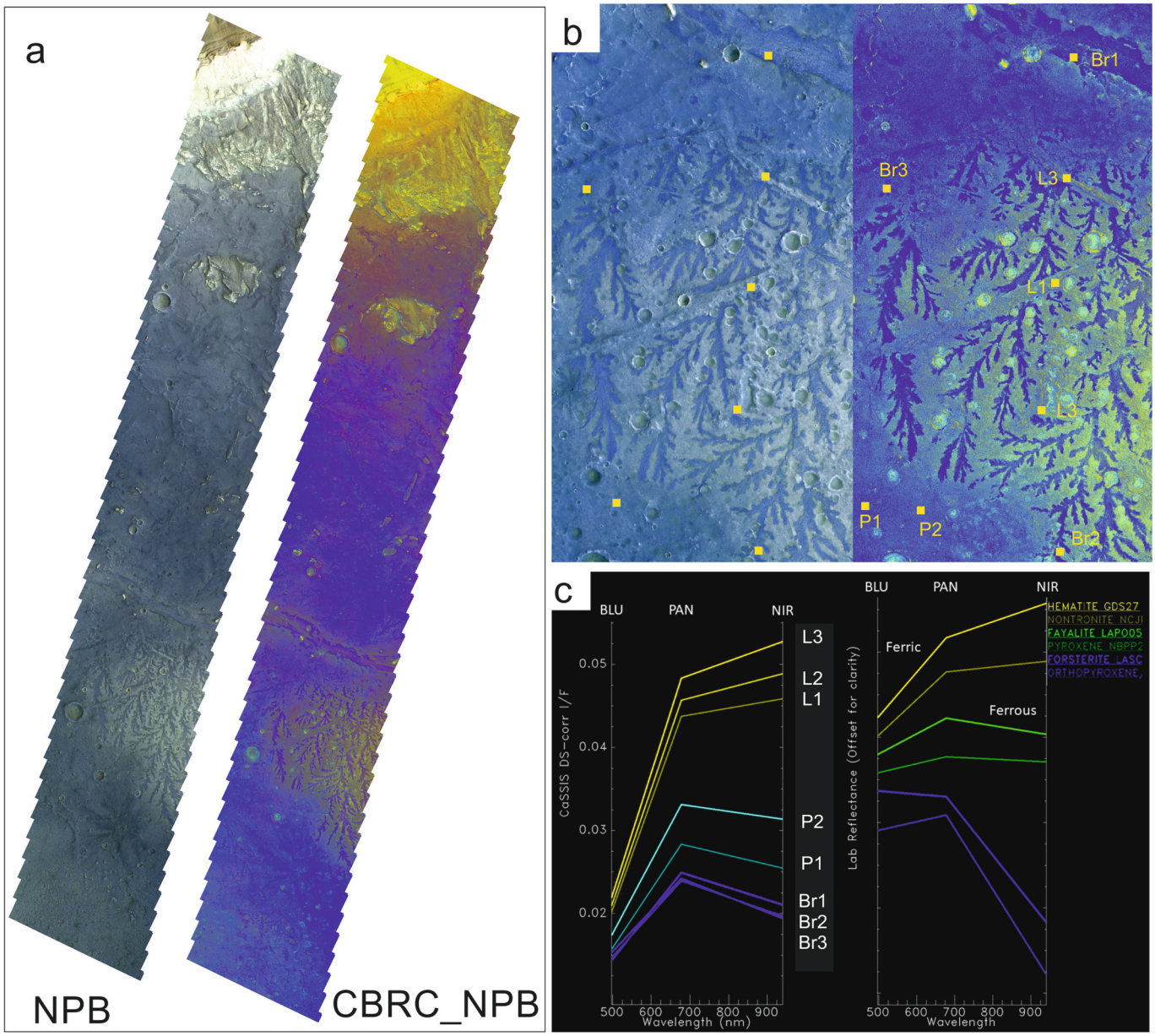

Fig. 15. (a) CaSSIS color images (#MY35_010430_024) in NIR-PAN-BLU filters as RGB and a color band ratio composite (CBRC-NPB) corresponding to CaSSIS filters ratio as following: NIR/PAN, PAN/BLU and PAN/NIR plotted as RGB (ESA/TGO/CaSSIS CC BY-SA 3.0 IGO). (b) Locations for which spectra are provided as examples are branched ridges (Br1 to Br3), light-toned plains (L1 to L3) and medium-toned plains (P1 and P2). (c) Comparison between these example spectra (left) with spectra from laboratory measurements (right).

inertia than underlying terrains (Fig. 14). The composition of branched ridges is likely basaltic based on their CaSSIS multispectral characteristics, and comparable to other areas on Mars where a basaltic composition can be generally inferred from a bluish color, (Delamere et al., 2010). Overall, these characteristics point toward a basaltic composition such as in lava flows.

Lava flows can explain many characteristics of the observed ridges, such as the presence of terminal lobes and preserved levees, localization along dikes, rubbly texture and lack of internal bedding, high thermal inertia and basaltic composition. The regional context is also mostly volcanic and lack fluvial landforms. Crater A has been filled by a huge amount of deformed material that we interpret as volcanic flows (Fig. 5). Crater B ejecta have also been buried below a material forming smooth plains Sp1 that can be interpreted as a volcanic filling. The polygonal cracks observed within Sp1 questions its origin, given that sedimentary rocks can display regular cracks, but similar cracks have been observed extensively in the volcanic region of Cerberus Fossae (e.g., Ryan and Christensen, 2012). In addition, none of the craters A and B displays any sign of fluvial erosion and filling while Sp1 is stratigraphically younger than both craters.

Could other types of flow explain dendritic ridges better than lava flows? Mud volcanoes are thought to exist on Mars in the northern plains (Oehler and Allen, 2010; Brož et al., 2020). The low viscosity of mud could potentially explain a higher degree of branching. However, mud volcanoes elsewhere on Mars (Cuřín et al., 2023) are made of fine-grained material and thus would be dark in night-time THEMIS images, or of low thermal inertia, in contrast with the studied ridges. They are made of soft muddy material also distinct from the ridges' rubbly texture. Mass wasting such as landslides and gravity flows could potentially explain the rubbly texture, but they commonly do not form as digitate flows. In addition, the local slope is low (0.3° at most) and no surrounding topography could explain gravity flows over such flat

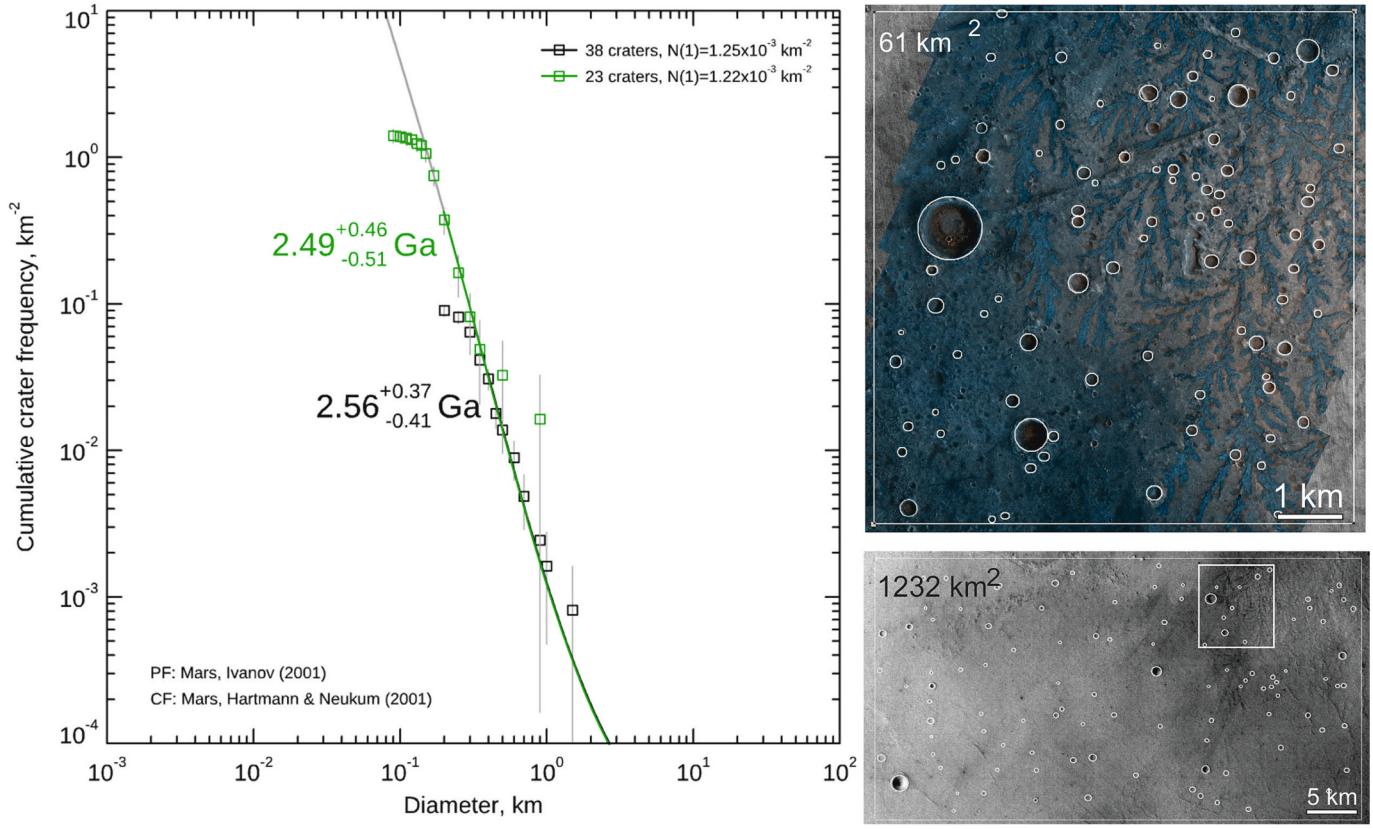

Fig. 16. Crater distribution using HRSC scale on 1232 km^2 (lower right image) and CaSSIS image on 61 km^2 (top right image). For the HRSC image, 111 craters from 200 m to 1.55 km were measured. The downturn at <300 m is likely related to image quality. The age estimation made using the 38 craters >400 m gives an age of 2.56 Gy −0.41/+0.37. For CaSSIS image, 86 craters from 100 m to 1 km were measured. The age estimation made for the 23 craters >200 m gives an age of 2.49 Gy −0.51/+0.49. Note that the upturn of the crater distribution plot above the isochron at diameter > 700 m is due to the presence of a single ~1 km diameter crater, which has a low effect on the statistical fit.

terrains. Layered impact ejecta can locally display lobate patterns, but no branching pattern has ever been reported in such a context. Ejecta are emplaced by processes of high energy and high velocity, so they would show a major direction of flow (such as southward assuming crater B is the source), which does not explain the opposite northward or the eastward orientation of the some of the branched ridges and their link with local fractures in area 1. Lastly, an explanation as (bio)chemical precipitates (De Blasio, 2022) seems to us unlikely given the difference of scale from dendritic precipitates (such as manganese dendrites formed at centimeter scale) as well as due to the recent age of these processes in the Amazonian, well after the Noachian era during which life could potentially have formed.

Yet, lava flows can present digitations, but they do not typically appear as branched as observed here. Lava flows can display braiding as frequently observed for low viscosity pahoehoe flows in Hawaii (Dietterich and Cashman, 2014). Here, the rubbly texture would better point toward a'a type of flows, which are usually more viscous and colder than pahoehoe flows. Comparisons made with the a'a flows of the 1961 Askja eruption in Iceland (Blasizzo et al., 2022) show the same type of rubbly texture, size of flows and local digitate nature, but their extent is much more limited (Fig. 19).

A first scenario to explain the extreme digitate shape of these flows could come from the putative presence of pre-existing fluvial valleys, later filled by lava flows after a topographic tilt to explain the filling in an opposite direction, toward valley heads. Such a case is frequently observed on Earth when lavas flow within pre-existing fluvial valleys and surrounding rocks are sediments that are soft enough to be eroded before the lava flows, producing an inversion of the preexisting channels relief (e.g., Pain and Ollier, 1995; Wyk de Vries Van et al., 2022). This hypothesis could explain the dendritic pattern without requiring sedimentary deposits. Nevertheless, the topography of the surrounding light-toned plains does not show any pre-existing river systems at this stratigraphic level. These locations are among the deepest of Antoniadi basin, and so it is difficult to explain that fluvial erosion would have been able to erode a location where sediments should accumulate, and would not have eroded the rims of craters A and B. Indeed, according to the stratigraphy, such fluvial erosion would postdate Sp1 plains, thus also the formation of both craters A and B, which are not affected by fluvial erosion.

A second scenario assumes that the digitate flows are peculiar lava flows producing this pattern. In such scenario, we have no definitive explanations for the reasons of the well-expressed branches. Nevertheless, digitate flows have been observed in subaqueous lava flows at Pico Island (Azores, Portugal) (Mitchell et al., 2008). This context is excluded for such a case on Mars, but Mitchell et al. (2008) mention that the density contrast below water would mimic density contrast related to lower Mars gravity. The recent eruptions of Nishinoshima volcano (Japan) in 2017 (Kaneko et al., 2019) display impressive digitate margins of a'a lava flows when reaching flat surfaces (Fig. 19) although those are not as dendritic as those observed at Antoniadi. More study of the composition of the ridges and of the regional context may help to understand these specific characteristics.

6. Conclusion

Antoniadi basin displays dark-toned dendritic ridges that could represent important examples of late-stage fluvial landforms if formed as inverted channels. However, careful observations of these branched

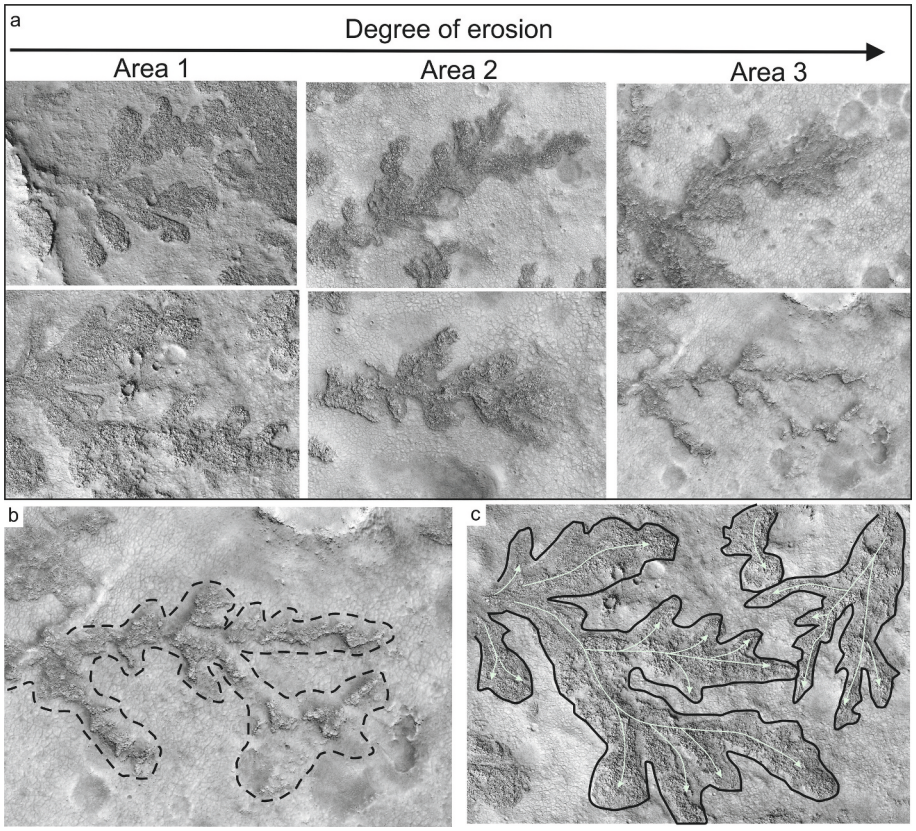

Fig. 17. (a) Close-ups on branched ridges from areas 1 (left) to 3 (right). Scale is the same in all images but images have been reoriented to provide better comparisons. We interpret the differences in shape to a difference of erosion, stronger going toward east, i.e. toward area 3. (b) Example of area 3 with dotted lines corresponding to presumed initial shape of ridges. The pattern is similar to branched ridges from area 1. (c) Interpretation of a branch of network as a flow formed by a distributary network.

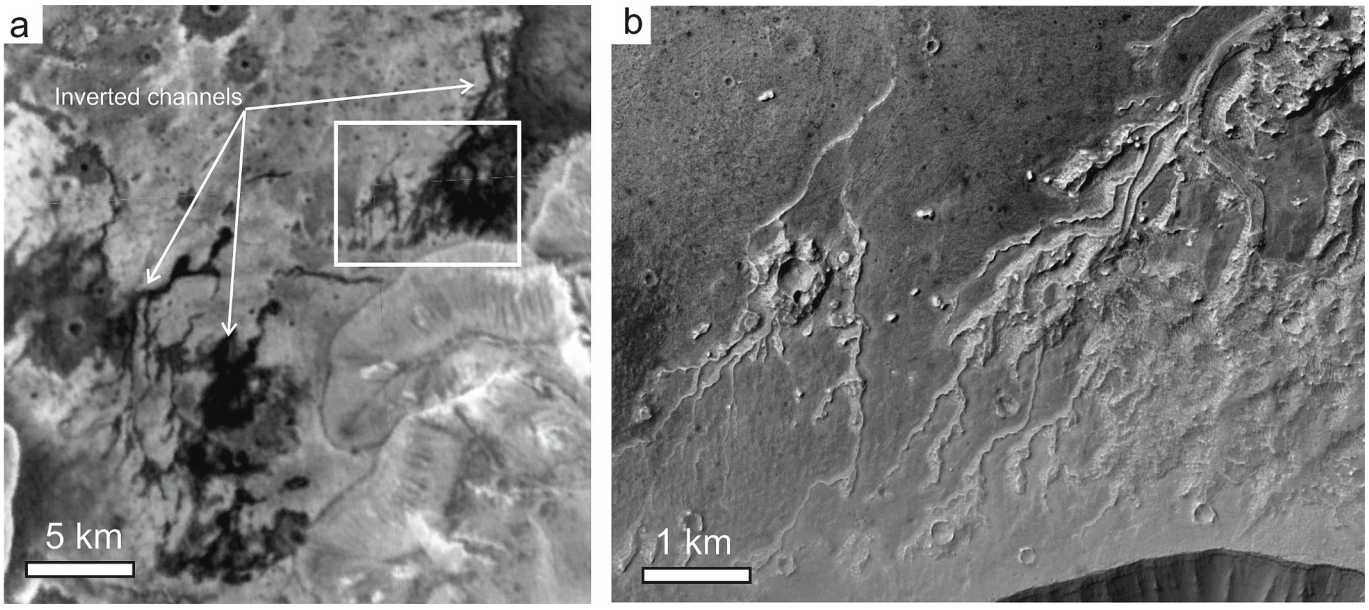

Fig. 18. (a) THEMIS night-time mosaic of inverted channels interpreted as fluvial on the plateau of Juventae Chasma. Inverted channels are narrow with dark tone indicating relatively low thermal inertia. (b) CTX mosaic of the same inverted channels.

ridges utilizing multiple datasets, providing morphologic, morphometric, thermophysical and color/multispectral constraints, show that they do not have characteristics consistent with fluvial channels. The pattern of ridges in Antoniadi basin lack downstream widening and, unlike contributory systems, have connected branch terminations, permissible in a distributary system. Furthermore, the dark ridges exhibit no evidence of layering suggestive of sedimentary deposition. Instead, they are dark, blue in color, have a rubbly texture and higher thermal inertia relative to their surroundings. Given a basaltic-predominant composition deduced from CaSSIS color/multispectral information, these overall characteristics are better explained by volcanic flows developed as distributary flows rather than an inversion of contributory fluvial channel deposits.

While the degree of branching of these flows is not common for lava

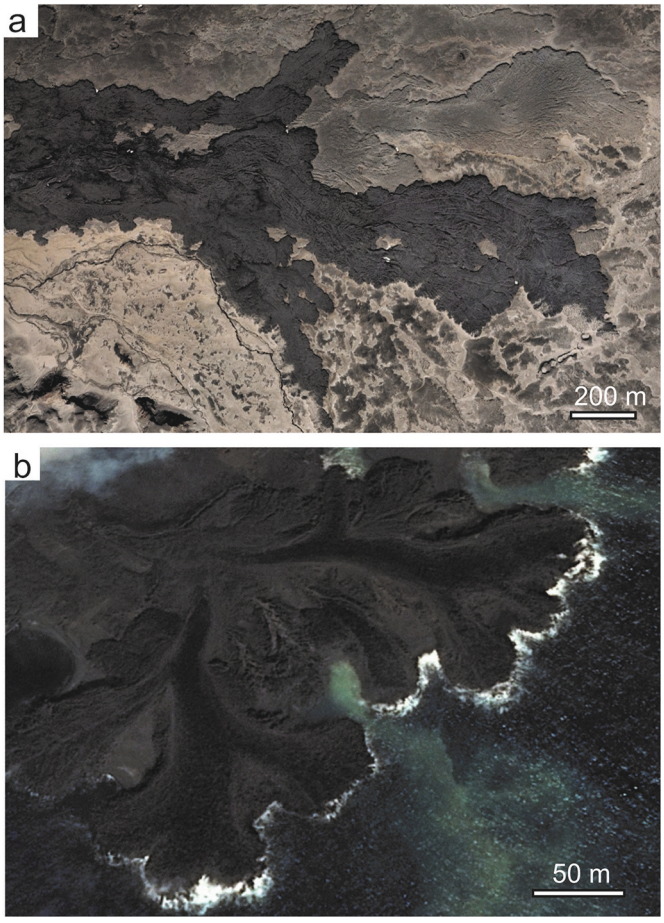

Fig. 19. (a) Orbital image from the a'a flows of the Askja 1961 eruption in Iceland (Google Earth, Maxar Technologies). (b) Orbital image of the Nishinoshima island volcano in Japan (Google Earth, CNES/Airbus).

flows on Earth or Mars, one explanation could be that lava flows formed within pre-existing valleys, forming inverted landforms (Zaki et al., 2020). Yet, the underlying topography does not present clear evidence of fluvial erosion. Local geological units that are stratigraphically older, including notably two large craters, do not display any signs of such activity. In addition, the fluvial scenario would also imply a tilt between the formation of rivers with a northward direction, and the subsequent filling by lava flows in the opposite direction. Given the overall context of the study area with many flow features and of dikes interpreted as volcanic, we favor an explanation of these patterns by distributary lava flows.

The term "equifinality" qualifies in geomorphology the fact that distinct processes can produce morphologically similar landforms (e.g., Haines-Young, 1982). Dendritic landforms conjures in our minds river networks. The example of the dendritic ridges in the Antoniadi basin shows that initial impressions can be incorrect, yet a comprehensive morphological study can reveal subtle differences that are key to an informed interpretation.

Declaration of Competing Interest

The authors declare that they have no known competing financial interests or personal relationships that could have appeared to influence the work reported in this paper.

Data availability

Data will be made available on request.

Acknowledgments

The data (CaSSIS, HRSC, CTX, HiRISE, MOLA) that support the findings of this study were obtained freely from the Planetary Data System (PDS) and Planetary Science Archive (PSA) and are publicly available online, respectively at https://pds.nasa.gov/index.shtml and https://archives.esac.esa.int/psa/. The authors wish to thank CaSSIS, MRO and HRSC science and instrument teams for data planning. NM, AG, SJC, and AN are supported by the French space agency CNES (Centre National d'Etudes Spatiales). LLT wishes to personally acknowledge funding and support from the Canadian NSERC Discovery Grant programme (RGPIN 2020-06418) and the Canadian Space Agency (CSA) Planetary and Astronomy Missions Co-Investigator programme (22EXPCOI3). Peter Fawdon is currently supported by the UK Space Agency on UK Space Agency grant ST/W002736/1 and was supported by The UK Science and Technology Facilities Council (STFC), by the British Geological Survey BUFI case studentship.

Appendix A. Supplementary data

Supplementary data to this article can be found online at https://doi.org/10.1016/j.icarus.2023.115735.

References

Blasizzo, A.Y., Ukstins, I.A., Scheidt, S.P., Graettinger, A.H., Peate, D.W., Carley, T.L., Moritz, A.J., Thines, J.E., 2022. Vikrahraun—the 1961 basaltic lava flow eruption at Askja, Iceland: morphology, geochemistry, and planetary analogs. Earth, Planets Space 74, 168.

Brož, P., Krýza, O., Wilson, L., Conway, S.J., Hauber, E., Mazzini, A., Raack, J., Balme, M. R., Sylvest, M.E., Patel, M.R., 2020. Experimental evidence for lava-like mud flows under Martian surface conditions. Nat. Geosci. 13, 403–407.

Burr, D.M., Williams, R.M.E., Wendell, K.D., Chojnacki, M., Emery, J.P., 2010. Inverted fluvial features in the Aeolis/Zephyria Plana region, Mars: formation mechanism and initial paleodischarge estimates. J. Geophys. Res. 115, E07011. https://doi.org/10.1029/2009JE003496.

Christensen, P.R., et al., 2004. The thermal emission imaging system (THEMIS) for the Mars 2001 odyssey mission. Space Sci. Rev. 110, 85–130.

Cuřín, V., Brož, P., Hauber, E., Markonis, Y., 2023. Mud flows in southwestern utopia Planitia, Mars. Icarus 389, 115266. https://doi.org/10.1016/j.icarus.2022.115266.

Davis, J.M., Balme, M., Grindrod, P.M., Williams, R.M.E., Gupta, S., 2016. Extensive Noachian fluvial systems in Arabia Terra: implications for early Martian climate. Geology 44 (10), 847–850.

De Blasio, F.V., 2022. The large dendritic morphologies in the Antoniadi crater (Mars) and their potential Astrobiological significance. Geosciences 2022 (12), 53. https://doi.org/10.3390/geosciences12020053.

Delamere, W.A., Tornabene, L.L., McEwen, A.S., Becker, K., Bergstrom, J.W., Bridges, N. T., Eliason, E.M., Gallagher, D., Herkenhoff, K.E., Keszthelyi, L., Mattson, S., McArthur, G.K., Mellon, M.T., Milazzo, M., Russell, P.S., Thomas, N., 2010. Color imaging of Mars by the high resolution imaging science experiment (HiRISE). Icarus 205 (1), 38–52. https://doi.org/10.1016/j.icarus.2009.03.012.

Devauchelle, O., Petroff, A.P., Seybold, H.F., Rothman, D.H., 2012. Ramification of stream networks. Proc. Natl. Acad. Sci. 109 (51), 20832–20836. https://doi.org/10.1073/pnas.1215218109.

Dietterich, H.R., Cashman, K.V., 2014. Channel networks within lava flows: formation, evolution, and implications for flow behavior. J. Geophys. Res. Earth Surf. 119, 1704–1724. https://doi.org/10.1002/2014JF003103.

Fawdon, P., 2016. The Volcanic Evolution of Syrtis Major Planum, Mars. Ph D thesis. The Open University. https://doi.org/10.21954/ou.ro.0000bbb9.

Fergason, R.L., Christensen, P.R., Kieffer, H.H., 2006. High-resolution thermal inertia derived from the thermal emission imaging system (THEMIS): thermal model and applications. J. Geophys. Res. 111, E12. https://doi.org/10.1029/2006JE002735.

Haines-Young, R.H., 1982. Equifinality, Multiple Working Hypotheses and the Study of Landforms. U. of Salford, Department of Geography, p. 13.

Hartmann, W.K., Neukum, G., 2001. Chronology and the evolution of Mars. Space Sci. Rev. 96, 165–194.

Hiesinger, H., Head III, J.W., 2004. The Syrtis Major Planum volcanic province: Synthesis from Mars Global Surveyor data. J. Geophys. Res.-PLanets 109, E01004. https://doi.org/10.1029/2003JE002143.

Hooshyar, M., Singh, A., Wang, D., 2017. Hydrologic controls on junction angle of river networks. Water Resour. Res. 53, 4073–4083. https://doi.org/10.1002/2016WR020267.

Iverson, R.M., 1997. The physics of debris flows. Rev. Geophys. 35, 245–296.

Kaneko, T., Maeno, F., Yasuda, A., Takeo, M., Takasaki, K., 2019. The 2017 Nishinoshima eruption: combined analysis using Himawari-8 and multiple high-resolution satellite images. Earth, Planets Space 71, 140. https://doi.org/10.1186/s40623-019-1121-8.

Kirk, R.L., Howington-Kraus, E., Redding, B., Galuszka, D., Hare, T.M., Archinal, B.A., Soderblom, L.A., Barrett, J.M., 2003. High-resolution topomapping of candidate

MER landing sites with Mars orbiter camera narrow-angle images: MER CANDIDATE LANDING SITE TOPOMAPPING. J. Geophys. Res.: Planets 108. https://doi.org/10.1029/2003JE002131.

Kirk, R.L., Howington-Kraus, E., Rosiek, M.R., Anderson, J.A., Archinal, B.A., Becker, K. J., Cook, D.A., Galuszka, D.M., Geissler, P.E., Hare, T.M., Holmberg, I.M., Keszthelyi, L.P., Redding, B.L., Delamere, W.A., Gallagher, D., Chapel, J.D., Eliason, E.M., King, R., McEwen, A.S., 2008. Ultrahigh resolution topographic mapping of Mars with MRO HiRISE stereo images: meter-scale slopes of candidate Phoenix landing sites. J. Geophys. Res. 113, E00A24. https://doi.org/10.1029/2007JE003000.

Malin, M.C., et al., 2007. Context camera investigation on board the Mars reconnaissance orbiter. J. Geophys. Res. 112, E05S04. https://doi.org/10.1029/2006JE002808.

Mangold, N., Ansan, V., Masson, Ph., Quantin, C., Neukum, G., 2008. Geomorphic study of fluvial landforms on the northern Valles Marineris plateau, Mars. J. Geophys. Res. 113. https://doi.org/10.1029/2007JE002985. E08009.

Mangold, N., Adeli, S., Conway, S., Ansan, V., Langlais, B., 2012. A chronology of early Mars climatic evolution from impact crater degradation. J. Geophys. Res.-Planets 117, E4. https://doi.org/10.1029/2011JE004005.

Mangold, N., Tornabene, L., Conway, S., Guimpier, A., Noblet, A., Fawdon, P., Hauber, E., Pommerol, A., Thomas, N., 2021. Viscous Flows Formed the Branched Ridges of Antoniadi Crater, Mars, EGU General Assembly Conference Abstracts, EGU21–5946.

McEwen, A.S., Eliason, E.M., Bergstrom, J.W., Bridges, N.T., Hansen, C.J., Delamere, W. A., Grant, J.A., Gulick, V.C., Herkenhoff, K.E., Keszthelyi, L., Kirk, R.L., Mellon, M.T., Squyres, S.W., Thomas, N., Weitz, C.M., 2007. Mars reconnaissance Orbiter's high resolution imaging science experiment (HiRISE). J. Geophys. Res. 112 (E5) https://doi.org/10.1029/2005je002605.

Melosh, H.J., 1989. Impact Cratering. A Geologic Process. Oxford Monographs on Geology and Geophysics Series no. 11, p. 245.

Michael, G.G., Neukum, G., 2010. Planetary surface dating from crater size–frequency distribution measurements: partial resurfacing events and statistical age uncertainty. Earth Planet. Sci. Lett. 294 (3–4), 223–229. https://doi.org/10.1016/j.epsl.2009.12.041.

Mitchell, N.C., Beier, C., Rosin, P.L., Quartau, R., 2008. Tempera lava penetrating water: submarine lava flows around the coasts of Pico Island. Azores. Geochem. Geophys. Geosyst. 9, Q03024. https://doi.org/10.1029/2007GC001725.

Neukum, G., et al., 2004. HRSC: the high resolution stereo camera of Mars express. ESA SP1240, 17–35.

Oehler, D.Z., Allen, C.C., 2010. Evidence for pervasive *mud* volcanism in Acidalia Planitia, Mars. Icarus. 527 (208), 636–657.

Pain, C.F., Ollier, C.D., 1995. Inversion of relief — A component of landscape evolution. Geomorphology 12, 151–165. https://doi.org/10.1016/0169-555X(94)00084-5.

Plescia, J.B., Golombek, M.P., 1986. Origin of planetary wrinkle ridges based on terrestrial analogues. Geol. Soc. Am. Bull. 97, 1289–1299.

Robbins, S.J., Hynek, B.M., Lillis, R.J., Bottke, W.F., 2013. Large impact crater histories of Mars: the effect of different model crater age techniques. Icarus 225, 173–185.

Ryan, A.J., Christensen, P.R., 2012. Coils and polygonal crust in the Athabasca Valles region, Mars, as evidence for a volcanic history. Science 336, 449–452.

Seybold, H.J., Kite, E., Kirchner, J.W., 2018. Branching geometry of valley networks on Mars and Earth and its implications for early Martian climate. Sci. Adv. 4 (6), eaar6692. https://doi.org/10.1126/sciadv.aar6692.

Smith, D.E., et al., 2001. Mars orbiter laser altimeter: experiment summary after the first year of global mapping of Mars. J. Geophys. Res. 106 (23), 23,689–23,722.

Strahler, A.N., 1952. Hypsometric (area-altitude) analysis of erosional topology. Geol. Soc. Am. Bull. 63 (11), 1117–1142.

Tanaka, K.L., Skinner, J.A., Dohm, J.M., Irwin, R.P., Kolb, E.J., Fortezzo, C.M., Platz, T., Michael, G.G., Hare, T.M., 2014. Geologic Map of Mars, Scale 1:20,000,000. U.S. Geological Survey Scientific Investigations Map SIM 3292. Available at. http://pubs.usgs.gov/sim/3292.

Thomas, N., Cremonese, G., Ziethe, R., Gerber, M., Brändli, M., Bruno, G., Erismann, M., Gambicorti, L., Gerber, T., Ghose, K., Gruber, M., Gubler, P., Mischler, H., Jost, J., Piazza, D., Pommerol, A., Rieder, M., Roloff, V., Servonet, A., Trottmann, W., Uthaicharoenpong, T., Zimmermann, C., Vernani, D., Johnson, M., Pelò, E., Weigel, T., Viertl, J., De Roux, N., Lochmatter, P., Sutter, G., Casciello, A., Hausner, T., Ficai Veltroni, I., Da Deppo, V., Orleanski, P., Nowosielski, W., Zawistowski, T., Szalai, S., Sodor, B., Tulyakov, S., Troznai, G., Banaskiewicz, M., Bridges, J.C., Byrne, S., Debei, S., El-Maarry, M.R., Hauber, E., Hansen, C.J., Ivanov, A., Keszthelyi, L., Kirk, R., Kuzmin, R., Mangold, N., Marinangeli, L., Markiewicz, W.J., Massironi, M., McEwen, A.S., Okubo, C., Tornabene, L.L., Wajer, P., Wray, J.J., 2017. The colour and stereo surface imaging system (CaSSIS) for the ExoMars trace gas orbiter. Space Sci. Rev. 212, 1897–1944. https://doi.org/10.1007/s11214-017-0421-1.

Tornabene, L.L., Seelos, F.P., Pommerol, A., et al., 2018a. Image simulation and assessment of the colour and spatial capabilities of the colour and stereo surface imaging system (CaSSIS) on the ExoMars trace gas orbiter. Space Sci. Rev. 214, 18. https://doi.org/10.1007/s11214-017-0436-7.

Tornabene, L.L., Watters, W.A., Osinski, G.R., Boyce, J.M., Ling, V., Harrison, T.N., McEwen, A.S., 2018b. A depth versus diameter scaling relationship for the best-preserved melt-bearing complex craters on Mars. Icarus. https://doi.org/10.1016/j.icarus.2017.07.003.

Vaucher, J., Baratoux, D., Mangold, N., Pinet, P., Kurita, K., Grégoire M., 2009. The volcanic history of central Elysium Planitia: implications for martian magmatism. Icarus, 204 (2), 418–442, doi:https://doi.org/10.1016/j.icarus.2009.06.032.

Watters, T.R., 1993. Compressional tectonism on Mars. J. Geophys. Res. 17, 049–17060.

Werner, S.C., 2008. The early Martian evolution — constraints from basin formation ages. Icarus 195, 45–60.

Williams, R.M.E., Malin, M.C., 2008. Sub-kilometer fans in Mojave Crater. Mars Mojave Crater 198 (2), 365–383.

Williams, R.M.E., Irwin, R.P., Zimbelman, J.R., 2009. Evaluation of paleohydrologic models for terrestrial inverted channels: implications for application to martian sinuous ridges. Geomorphology 107 (3–4), 300–315. https://doi.org/10.1016/j.geomorph.2008.12.015.

Wyk de Vries Van, B., Karatson, D., Gouard, C., Nemeth, K., Rapprich, V., Aydar, E., 2022. Inverted volcanic relief: its importance in illustrating geological change and its geoheritage potential. Intern. J. Geoherit. Parks 10, 47–83.

Zaki, A.S., Edgett, K.S., Gupta, S., Pajola, M., Davis, J.M., Hugues, C.M., Watkins, S., Valero, L., Grindrod, P.M., Thomas, N., Cremonese, G., Castelltort, S., 2020. Reconstructing the fluvial history of Antoniadi crater: Evidence for Noachian and Amazonian stream networks on Mars. AGU Fall meeting, abstract #P065-0010.

Zaki, A.S., Pain, C.F., Edgett, K.S., Castelltort, S., 2021. Global inventory of fluvial ridges on earth and lessons applicable to Mars. Earth-Sci. Rev. 216, 103561.